

**BM@N Note**  
**Production of  $\Lambda$  hyperons in**  
**4.0 and 4.5 A GeV carbon-nucleus interactions**

**Analysis team:** M.Kapishin, G.Pokatashkin,  
I.Rufanov, Yu.Stepanenko, V.Vasendina, A.Zinchenko

**Abstract**

Production of  $\Lambda$  hyperons in interactions of the carbon beam with the kinetic energy 4.0 and 4.5 AGeV with the *C, Al, Cu, Pb* targets was studied with the BM@M detector at the Nuclotron. The analysis procedure is described in details. Results on  $\Lambda$  hyperon yields have been obtained and compared with model predictions and data available.

**BM@N configuration in the carbon beam run**

The technical run of the BM@N detector was performed with the carbon beam in March 2017. The view of the BM@N setup used in the run is presented in Fig. 1 (left). The configuration of the central tracker was based on one plane of a forward silicon detector and six GEM stations combined from 5 GEM detectors with the size of 66x41 cm<sup>2</sup> and 2 GEM detectors with the size of 163x45 cm<sup>2</sup> [GEMTDR]. The tracking stations were arranged to have the beam passing through their centers (Fig. 1 (right)). Each successive GEM station was rotated by 180° around the vertical axis. It was done to have the opposite electron drift direction in the successive stations in order to avoid a systematic shift of reconstructed tracks due to the Lorentz angle in the magnetic field. The research program was devoted to measurements of inelastic reactions  $C+A \rightarrow X$  with the beam kinetic energy of 4.0 and 4.5A GeV and different targets: *C, Al, Cu, Pb*. The technical program of the run included the measurement of the carbon beam momentum in the central and outer tracker at different values of the magnetic field. Since the GEM tracker configuration was tuned to measure relatively high-momentum beam particles, the geometric acceptance for relatively soft decay products of strange  $V0$  particles was rather low.

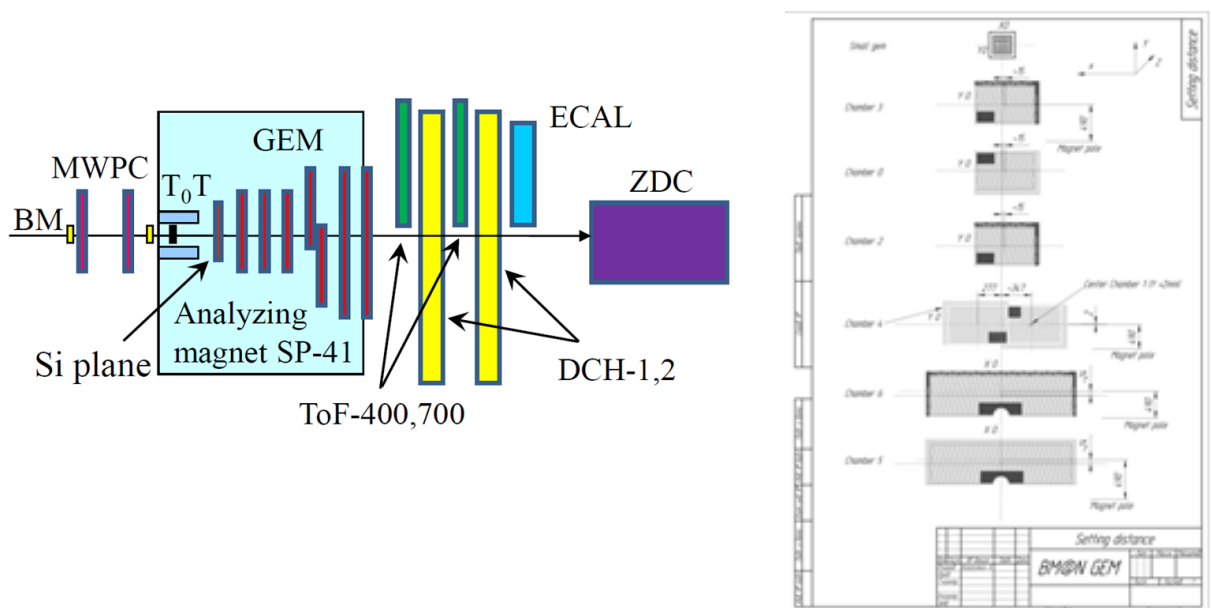
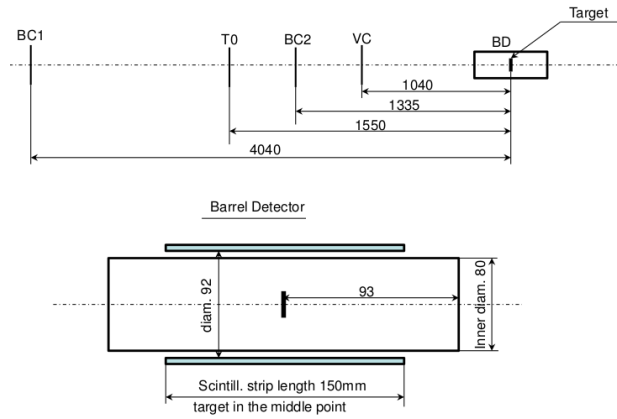


Fig. 1. Left plot: BM@N set-up in the carbon beam run. Right plot: configuration of the GEM detectors, see a more detailed plot at [GEMconf].



27

28 Fig.1b. Schematic view and positions of the beam counters, barrel detector and target.

29 In the present analysis the experimental data from the forward silicon detector, GEM detectors,  
 30 trigger barrel multiplicity detector, beam, veto and T0 counters were used. The positions of the  
 31 beam counters and trigger barrel detector and the target are given in Fig.1b. The carbon beam  
 32 intensity was few  $10^5$  per the spill, the spill duration was 2-2.5 sec. The magnetic field in the  
 33 center of the analyzing magnet was 0.61 T.

#### 34 Monte Carlo simulation and event reconstruction

35 The Monte Carlo event samples of C+A collisions were produced with the DCM-QGSM event  
 36 generator. The passage of particles through the setup volume was simulated with the GEANT  
 37 program integrated into the BmnRoot software framework. To properly describe the GEM  
 38 detector response in the magnetic field the microsimulation package Garfield++ was used. The  
 39 package gives very detailed description of the processes inside the GEM detector, including the  
 40 drift and diffusion of released electrons in electric and magnetic fields and the electron  
 41 multiplication in GEM foils, so that the output signal from the readout plane can be reproduced.  
 42 To speed up the simulation, dependencies of the Lorentz shifts and the charge distributions on  
 43 the readout planes on the drift distance were parameterized and used in the GEM digitization part  
 44 of the BmnRoot package. The details of the detector alignment, Lorentz shift corrections are  
 45 described in the paper [DeuteronPaper]. The track reconstruction method was based on the so-  
 46 called "cellular automaton" approach [CBM1]. The tracks found were used to reconstruct  
 47 primary and secondary vertices using the "KF-particle" formalism [CBM2].  $\Lambda$  hyperons were  
 48 reconstructed using their decay mode into two oppositely-charged tracks. The signal event  
 49 topology (decay of a relatively long-lived particle into two tracks) defined the selection criteria:  
 50 small track-to-track separation in the decay vertex, relatively large decay length of the mother  
 51 particle. Since particle identification was not used in the analysis, all positive tracks were  
 52 considered as protons and all negative as  $\pi^-$ .

#### 53 Event selection criteria:

- 54 1. Number of tracks in selected events: positive  $\geq 1$ , negative  $\geq 1$ ;
- 55 2. Beam halo, pile-up suppression within the readout time window: number of signals in the  
 56 start detector: T0=1, number of signals in the beam counter: BC2=1, number of signals in  
 57 the veto counter around the beam: Veto=0;

58 3. Trigger condition in the barrel detector: number of signals  $BD \geq 2$  or  $BD \geq 3$  (run  
59 dependent).

60 The suppression factors of reconstructed events  $\varepsilon_{pileup}$  due to selection criteria 2 applied to  
61 eliminate beam halo and pile-up events in interactions of the 4.0 and 4.5 AGeV carbon beam  
62 with the *C*, *Al*, *Cu*, *Pb* targets are given in Table 1.

63 Table 1.  $\varepsilon_{pileup}$  suppression factors.

Selection	4 AGeV	4.5 AGeV
T0==1	+	+
BC2==1	+	+
Veto==0	+	+
<i>C</i>	0.674	0.529
<i>Al</i>	0.740	0.618
<i>Cu</i>	0.779	0.621
<i>Pb</i>	0.784	0.686

64 The total suppression factors are applied to reduce the recorded beam fluxes and luminosities  
65 which are summarized in Table 2.

66 Table 2. Number of triggered events, beam fluxes and integrated luminosities collected in  
67 interactions of the carbon beam of 4.0 and 4.5 AGeV with different targets.

Interactions, target thickness	Number of triggers / $10^6$	Integrated beam flux / $10^7$	Integrated luminosity / $10^{30} \text{ cm}^{-2}$
4 AGeV, <i>C+C</i> (9 mm)	3.98	6.07	6.06
4 AGeV, <i>C+Al</i> (12 mm)	3.81	3.31	2.39
4 AGeV, <i>C+Cu</i> (5 mm)	4.77	4.71	2.00
4 AGeV, <i>C+Pb</i> (10 mm)	0.67	0.67	0.22

68

Interactions, target thickness	Number of triggers / $10^6$	Integrated beam flux / $10^7$	Integrated luminosity / $10^{30} \text{ cm}^{-2}$
4.5 AGeV, <i>C+C</i> (9 mm)	2.93	4.70	4.69
4,5 AGeV, <i>C+Al</i> (12 mm)	3.58	4.98	3.60
4.5 AGeV, <i>C+Cu</i> (5 mm)	5.30	7.21	3.06
4.5 AGeV, <i>C+Pb</i> (10 mm)	2.33	2.58	0.84

69

70  **$\Lambda$  hyperon selection criteria:**

- 71 • Each track has at least 4 hits in Si and GEM detectors (7 detectors in total), where hit is a
- 72 combination of two strip clusters on both readout sides ( $X$  and  $X'$  views) on each detector
- 73 [GEMTDR]
- 74 • Momentum range of positive tracks:  $p_{pos} < 3.9, 4.4$  GeV/ $c$  for 4.0 and 4.5 AGeV carbon
- 75 beam data, respectively
- 76 • Momentum range of negative tracks:  $p_{neg} > 0.3$  GeV/ $c$
- 77 • Distance of the closest approach of  $V0$  decay tracks (distance in X-Y plane between  $V0$
- 78 decay tracks at  $Z=Z_{V0}$ ):  $dca < 1$  cm
- 79 • Distance between  $V0$  and primary vertex:  $path > 2.0-2.5$  cm

80 Distributions of the experimental primary vertex are given in Fig.6. Distributions of kinematic  
 81 and spatial parameters used for the  $\Lambda$  hyperon selection are presented in Fig.7. Spectra of the  
 82 invariant mass of  $(p, \pi^-)$  reconstructed in interactions of 4.0 and 4.5 AGeV carbon beam with  
 83 different targets are shown in Fig.10a and 10b, respectively. To extract  $\Lambda$  hyperon signal, the  
 84 distributions were fitted to the 4<sup>th</sup> degree Legendre polynomial (background) in the mass range  
 85 1.08-1.18 GeV/ $c^2$ . To avoid a bias due to possible deviation of the peak from the Gaussian shape,  
 86 the numbers of  $\Lambda$  hyperons were determined not from the Gaussian fit but from the content of the  
 87 background-subtracted histogram bins within 1107.5-1125 MeV/ $c^2$  mass window. This mass  
 88 window where  $\Lambda$  signal contributes was excluded from the Legendre polynomial fit.  $\Lambda$  signals in  
 89 intervals of the transverse momentum  $p_T$  and rapidity  $y_{lab}$  were reconstructed using similar fit  
 90 procedure, i.e. the numbers of  $\Lambda$  hyperons were calculated within 1107.5-1125 MeV/ $c^2$  window  
 91 as excess signals relative to background calculated from fits of  $(p, \pi^-)$  mass spectra to the 4th  
 92 Legendre polynomial in  $p_T$  and  $y_{lab}$  intervals. The error of the  $\Lambda$  signal includes the uncertainty of  
 93 the background subtraction. The statistical and systematic errors were calculated according to the  
 94 formula:  $sig=hist-bg$ ,  $err(stat)=\sqrt{hist}$ ,  $err(syst)=\sqrt{(0.5*bg)}$ , assuming that the background was  
 95 estimated with the uncertainty of  $\sqrt{(0.5*bg)}$ . If the variation of the background shape due to use  
 96 of the 3th degree Legendre polynomial gave larger uncertainties than  $\sqrt{(0.5*bg)}$ , the largest  
 97 uncertainty was taken as a systematic error. The statistics of  $\Lambda$  hyperons reconstructed in  $C+C$ ,  
 98  $C+Al$ ,  $C+Cu$ ,  $C+Pb$  interactions in bins of  $y_{lab}$  and  $p_T$  are summarized in Fig.11a,b and in Tables  
 99 3a and 3b for 4.0 AGeV and 4.5 AGeV carbon beam data, respectively.

100 Table 3a. Reconstructed signals of  $\Lambda$  hyperons in bins of  $y_{lab}$  and  $p_T$  in 4.0 AGeV carbon-target  
 101 interactions. The first error presents the statistical uncertainty, the second error is systematic.

Target $y$ inter. in lab. frame	$Y$				Target $p_T$ interval	$p_T$			
	$C$	$Al$	$Cu$	$Pb$		$C$	$Al$	$Cu$	$Pb$
1.2-1.45	225±35±23	279±52±35	610±66±43	133±27±18	0.1-0.3	463±58±38	427±77±52	691±89±60	164±35±23
1.45-1.65	343±41±26	475±61±40	643±73±48	110±28±19	0.3-0.55	380±52±34	538±76±51	787±89±60	159±34±22
1.65-1.85	334±48±31	420±69±46	604±79±54	102±31±20	0.55-0.8	285±40±25	462±61±40	450±70±47	91±27±18
1.85-2.1	284±52±35	371±72±49	375±79±55	111±30±19	0.8-1.05	57±20±13	118±32±21	304±39±25	43±13±9

102 Table 3b. Reconstructed signals of  $\Lambda$  hyperons in bins of  $y_{lab}$  and  $p_T$  in 4.5 AGeV carbon-target  
 103 interactions. The first error presents the statistical uncertainty, the second error is systematic.

104

105

Target $y$ Inter. in lab. frame	$y$				Target $p_T$ interval	$p_T$			
	$C$	$Al$	$Cu$	$Pb$		$C$	$Al$	$Cu$	$Pb$
1.25-1.5	170±38±25	316±67±46	640±81±55	292±69±47	0.1-0.3	141±58±40	270±91±63	674±103±70	211±79±55
1.5-1.7	248±42±28	555±76±50	635±87±59	304±69±47	0.3-0.55	306±52±34	632±92±63	803±104±71	418±81±56
1.7-1.9	242±48±32	570±84±56	626±93±64	417±70±48	0.55-0.8	239±43±28	549±79±53	698±88±60	312±69±47
1.9-2.15	79±54±37	223±91±62	650±98±67	57±70±49	0.8-1.05	54±24±16	211±48±32	375±55±36	129±43±28

106 To evaluate the  $\Lambda$  hyperon acceptance and reconstruction efficiencies, minimum bias interactions  
107 of 4.0 and 4.5A GeV carbon beam with  $C$ ,  $Al$ ,  $Cu$ ,  $Pb$  targets were generated with the DCM-  
108 QGSM generator. The generated particles were traced through the BM@N geometry using the  
109 GEANT simulation and reconstructed using the BmnRoot software framework. Experimental  
110 and Monte Carlo distributions of the track multiplicity, number of tracks reconstructed in the  
111 primary vertex and number of hits per track are presented in Fig.2a and 2b for 4.0 and 4.5 AGeV  
112 carbon beam data, respectively. Distributions of the transverse momentum  $p_T$  and total  
113 momentum  $p$  of reconstructed positive and negative particles in data and simulation are shown in  
114 Fig.3a and 3b for interactions of 4.0 and 4.5 AGeV carbon beam, respectively.

115 To reproduce the detector effects in the reconstruction efficiency the simulated products of  $\Lambda$   
116 hyperon decays ( $p, \pi^-$ ) were embedded into real experimental events of  $C+C$ ,  $C+Al$ ,  $C+Cu$ ,  
117  $C+Pb$  interactions. Simulated amplitude signals in the Forward Silicon and GEM detectors were  
118 convoluted with amplitudes of the experimental signals in these detectors. Two-dimensional  $X/Y$   
119 efficiency distributions in 6 GEM stations measured with reconstructed experimental tracks are  
120 shown in Fig.4. For each station they were estimated using the following approach:

- 121 1. Select good quality tracks with the number of hits per track (excluding the station under  
122 study) not less than  $N$ ;
- 123 2. Check that track crosses the detector area, if yes, add one track to the denominator;
- 124 3. If there is a hit in the detector, which belongs to the track, add one track to the numerator;
- 125 4. Detector efficiency = sum of tracks in numerator / sum of tracks in denominator.

126 These efficiencies were applied to reduce the number of hits of embedded tracks of  $\Lambda$  decay  
127 products.

128 The experimental distribution of GEM hit residuals to tracks is presented in Fig.5. The  
129 corresponding distribution for embedded tracks of  $\Lambda$  decay products is also shown in Fig 5. The  
130 RMS of distributions are in a reasonable agreement. The invariant mass spectrum of ( $p, \pi^-$ ) pairs  
131 reconstructed in the experimental events of  $C+Cu$  interactions with embedded  $\Lambda$  hyperon decay  
132 products is illustrated in Fig.8. The  $\Lambda$  signal is reproduced by a Gaussian function with the sigma  
133 of 2.4 MeV, which is consistent with the sigma of the experimental  $\Lambda$  distribution of 2.6 MeV.  
134 Variation of sigma of the experimental  $\Lambda$  signal and embedded  $\Lambda$  signal reconstructed in bins of  
135  $p_T$  is illustrated in Fig.9. To estimate statistical fluctuations of the experimental  $\Lambda$  signal, the  
136 Legendre polynomial fit is performed for the mass distribution shifted at a half of the mass bin  
137 ( $1.25 \text{ MeV}/c^2$ ). The difference in sigma is presented as error bands in the plots.

138 The resulting  $\Lambda$  reconstruction efficiency is the ratio of the number of reconstructed  $\Lambda$  hyperons  
139 to the number of generated ones in the intervals of ( $p_T, y$ ), where  $y$  is measured in the laboratory  
140 frame ( $y_{lab}$ ). The reconstruction efficiency can be decomposed into the following components:

141  $\varepsilon_{rec} = \varepsilon_{acc} \cdot \varepsilon_{emb+cuts}$ . The definition of every term is given in Table 4 and their determination  
 142 procedure is as follows.

143 Reconstructed primary vertices from experimental events were taken to serve as the interaction  
 144 point for DCM-QGSM generated events with produced  $\Lambda$ s. After the event simulation and  
 145 reconstruction the successfully reconstructed  $\Lambda$  was counted in the numerator  $N_{rec}$  and the  
 146 procedure continued with the next experimental event. In the opposite case, the current vertex  
 147 was used for the next MC event. The "successful reconstruction" means that the reconstructed  $\Lambda$   
 148 mass was within  $\pm 5$  MeV window around the table value and the reconstructed hyperon  
 149 "matches" with the generated one, i.e. its momentum components are within  $\pm 0.1$  and  $\pm 0.15$   
 150 GeV/c window from the true ones for  $p_x$  ( $p_y$ ) and  $p_z$ , respectively, and rapidity within  $\pm 0.2$ . The  
 151 detector acceptance was taken as  $N_{rec} / N_{gen}$ , where  $N_{gen}$  is the total number of MC events tried.

152 The accepted hyperons were used for the embedding procedure as follows. Monte Carlo digits  
 153 originated from  $\Lambda$  decay products were added to respective experimental events (as explained  
 154 above) and the reconstruction was performed again for such mixed data. This allowed us to take  
 155 into account many real-life effects (GEM efficiency, zero suppression, event pile-up). A fraction  
 156 of successfully reconstructed (in the explained above sense) embedded  $\Lambda$  after applying  
 157 kinematic and spatial cuts gave the "embedding and selection cuts" efficiency with respect to the  
 158 number of accepted ones from above.

159 Table 4. Decomposition of the  $\Lambda$  hyperon reconstruction efficiency.

Reconstruction efficiency	$\varepsilon_{rec} = \varepsilon_{acc} \cdot \varepsilon_{emb+cuts}$
$\Lambda$ geometrical acceptance in GEM detectors	$\varepsilon_{acc} = N_{acc}(y, p_T) / N_{gen}(y, p_T)$
Efficiency of reconstruction of embedded $\Lambda$ after applying kinematic and spatial cuts	$\varepsilon_{emb+cuts} = N_{emb+cuts}(y, p_T) / N_{acc}(y, p_T)$

160 To get 1-dimensional distributions of the full reconstruction efficiency in bins of  $p_T$  ( $y$ ) the  
 161 summation is done over  $y$  ( $p_T$ ) bins according to the formulae:

162 
$$\varepsilon_{rec}(p_T) = \sum_y N_{rec}(y, p_T) / \sum_y (N_{rec}(y, p_T) / \varepsilon_{rec}(y, p_T))$$
  
 163 
$$\varepsilon_{rec}(y) = \sum_{p_T} N_{rec}(y, p_T) / \sum_{p_T} (N_{rec}(y, p_T) / \varepsilon_{rec}(y, p_T))$$

164 The same approach is used to calculate 1-dimensional distributions of the acceptance and  
 165 "embedding and selection cuts" efficiency. The actual values of the efficiencies ( $\varepsilon_{acc}$ ,  $\varepsilon_{emb+cuts}$ )  
 166 and combined reconstruction efficiencies  $\varepsilon_{rec}$  calculated in the  $y$  and  $p_T$  bins are shown in Figs.  
 167 12a and 12b for 4.0 AGeV  $C+C$  and  $C+Cu$  interactions, respectively.

168 The trigger efficiency  $\varepsilon_{trig}$  calculated for events with reconstructed  $\Lambda$  hyperons in interactions of  
 169 carbon beam with different targets is given in Table 5. The trigger efficiency was evaluated by a  
 170 convolution of the GEANT simulation of the trigger BD detector response to DCM-QGSM  
 171 events with reconstructed  $\Lambda$  hyperons and the GEANT simulation of delta electrons produced by  
 172 the carbon beam in the  $C$ ,  $Al$ ,  $Cu$ ,  $Pb$  targets which were found to be the dominant source of delta  
 173 electrons. The dependence of the trigger efficiency on the collision impact parameter is  
 174 presented in Fig.12c for interactions of the carbon beam with the  $C$ ,  $Al$ ,  $Cu$ ,  $Pb$  targets. The  
 175 systematic errors in Table 5 cover: 1) the contribution of delta electrons background produced in

176 the simulated targets with the fractional thickness from 0.5 to 1 of the real targets; 2) the spread  
 177 of the trigger efficiency values calculated for different  $y$  and  $p_T$  bins of reconstructed  $\Lambda$  hyperons;  
 178 3) change in the trigger efficiency after adjustment (reweighting) of the simulated track  
 179 multiplicity to the experimental distributions shown in Fig. 2a,b. The trigger efficiency obtained  
 180 in simulation was cross checked by the analysis of data samples with the reduced trigger  
 181 requirements:  $BD \geq 1$  for  $C+C$  interactions and  $BD \geq 2$  for  $C+Al$  and  $C+Cu$  interactions. The  
 182 evaluated efficiencies for events with reconstructed  $\Lambda$   $\varepsilon(BD \geq 2)/\varepsilon(BD \geq 1, C+C) = 0.90$ ,  
 183  $\varepsilon(BD \geq 3)/\varepsilon(BD \geq 2, C+Al, C+Cu) = 0.95$  are consistent with the trigger efficiencies calculated  
 184 using simulated events.

185 Table 5. Trigger efficiency evaluated for events with reconstructed  $\Lambda$  hyperons in interactions of  
 186 the carbon beam with  $C$ ,  $Al$ ,  $Cu$ ,  $Pb$  targets. The last row shows the trigger efficiency averaged  
 187 over the data samples with trigger conditions  $BD \geq 2$  and  $BD \geq 3$ .

Trigger / Target, 4.0 AGeV	$C$	$Al$	$Cu$	$Pb$
$\varepsilon_{trig} (BD \geq 2)$	0.80±0.02			
$\varepsilon_{trig} (BD \geq 3)$		0.87±0.02	0.92±0.02	0.95±0.02

188

Trigger / Target, 4.5 AGeV	$C$	$Al$	$Cu$	$Pb$
$\varepsilon_{trig} (BD \geq 2)$	0.80±0.02			
$\varepsilon_{trig} (BD \geq 3)$		0.83±0.02	0.91±0.02	0.94±0.02

189 Distributions of the impact parameters of minimum bias interactions generated with the DCM-  
 190 QGSM, UrQMD and PSHD models are shown in Fig.12d. The impact parameter distributions of  
 191 generated events with  $\Lambda$  hyperons as well as the impact parameters of simulated events with  
 192 reconstructed  $\Lambda$  hyperons are presented for comparison. The  $\Lambda$  reconstruction requirements and  
 193 the trigger conditions do not change much the impact parameter distributions. The mean values  
 194 of the impact parameters for events with  $\Lambda$  hyperons generated in  $C+C$ ,  $C+Al$ ,  $C+Cu$ ,  $C+Pb$   
 195 interactions by the DCM-QGSM model are presented in Table 6.

196 Table 6. Mean impact parameters of min. bias  $C+C$ ,  $C+Al$ ,  $C+Cu$  and  $C+Pb$  interactions  
 197 generated by the DCM-QGSM model.

MC	$b$ , fm ( $C+C$ )	$b$ , fm ( $C+Al$ )	$b$ , fm ( $C+Cu$ )	$b$ , fm ( $C+Pb$ )
All min bias events	3.76	4.36	5.13	6.6
Events with $\Lambda$	2.80	3.08	3.58	4.8
Events with rec. $\Lambda$	2.71	3.18	3.88	5.2

198 The inclusive cross section  $\sigma_\Lambda$  and yield  $Y_\Lambda$  of  $\Lambda$  hyperon production in  $C+C$ ,  $C+Al$ ,  $C+Cu$ ,  
 199  $C+Pb$  interactions are calculated in bins of  $y$  ( $p_T$ ) according to the formulae:

$$\sigma_\Lambda(y) = \sum p_T [N_{rec}^\Lambda(y, p_T) / (\varepsilon_{rec}(y, p_T) \cdot \varepsilon_{trig} \cdot \varepsilon_{pileup} \cdot L)] \quad Y_\Lambda(y) = \sigma_\Lambda(y) / \sigma_{inel}$$

$$\sigma_\Lambda(p_T) = \sum y [N_{rec}^\Lambda(y, p_T) / (\varepsilon_{rec}(y, p_T) \cdot \varepsilon_{trig} \cdot \varepsilon_{pileup} \cdot L)] \quad Y_\Lambda(p_T) = \sigma_\Lambda(p_T) / \sigma_{inel}$$

200 where  $L$  is the luminosity (Table 2),  $N_{rec}^{\Lambda}$ —the number of reconstructed  $\Lambda$  hyperons (Tables  
 201 3a,3b),  $\varepsilon_{rec}$ —the combined efficiency of the  $\Lambda$  hyperon reconstruction,  $\varepsilon_{trig}$ —the trigger efficiency  
 202 (Table 5),  $\varepsilon_{pileup}$ —the beam halo and pile-up suppression factor (Table 1),  $\sigma_{inel}$ —the cross section  
 203 for minimum bias inelastic  $C+A$  interactions (Table 7). The cross section for inelastic  $C+C$   
 204 interactions is taken from the measurement [AngelovCC]. The cross sections for inelastic  $C+Al$ ,  
 205  $C+Cu$ ,  $C+Pb$  interactions are taken from the predictions of the DCM-QGSM model which are  
 206 consistent with the results calculated by the formula:  $\sigma_{inel} = \pi R_0^2 (A_P^{1/3} + A_T^{1/3})^2$ , where  $R_0 = 1.2$   
 207 fm is an effective nucleon radius,  $A_P$  and  $A_T$  are atomic numbers of the beam and target nucleus  
 208 [HadesL0]. The uncertainties for  $C+Al$ ,  $C+Cu$ ,  $C+Pb$  inelastic cross sections are estimated by  
 209 using the alternative formula:  $\sigma_{inel} = \pi R_0^2 (A_P^{1/3} + A_T^{1/3} - b)^2$  with  $R_0 = 1.46$  fm and  $b = 1.21$   
 210 [AngelovCC].

211 Table 7. Inelastic cross sections for carbon-nucleus interactions.

Interaction	$C+C$	$C+Al$	$C+Cu$	$C+Pb$
Inelastic cross section, mb	830±50	1260±50	1790±50	3075±50

212 The yields of  $\Lambda$  hyperons in minimum bias  $C+C$ ,  $C+Al$ ,  $C+Cu$ ,  $C+Pb$  interactions are measured  
 213 in the kinematic range on the  $\Lambda$  transverse momentum of  $0.1 < p_T < 1.05$  GeV/c and the  $\Lambda$  rapidity  
 214 in the laboratory frame of  $1.2 < y_{lab} < 2.1$  for 4.0 AGeV data ( $1.25 < y_{lab} < 2.15$  for 4.5 AGeV data).  
 215 The rapidity of the beam-target nucleon-nucleon CM system calculated for an interaction of the  
 216 carbon beam with the kinetic energy of 4.0 (4.5) GeV/nucleon with a fixed target is  $y_{CM}=1.17$   
 217 (1.22). The  $\Lambda$  rapidity range for 4.5 AGeV data is shifted at +0.05 to get approximately the same  
 218  $y^*$  range in the CM system as for 4.0 AGeV data. The transformation of the  $y$  distribution to  
 219 c.m.s. gives  $y^*=y_{lab}-y_{CM}$ . The differential spectra of the  $\Lambda$  yields in  $y_{lab}$  are measured in the  $\Lambda$   
 220 transverse momentum range of  $0.1 < p_T < 1.05$  GeV/c. The corrected differential  $y^*$  spectra of  $\Lambda$   
 221 hyperon yields are presented in Figs. 13a and 13b for 4.0 AGeV and 4.5 AGeV carbon beam  
 222 energies, respectively. The corrected differential  $p_T$  spectra of  $\Lambda$  hyperon yields are presented in  
 223 Figs. 14a and 14b. The predictions of the DCM-QGSM, URQMD and PHSD models are shown  
 224 for comparison. In Fig.15a and 15b the measured spectra of the  $\Lambda$  yields in  $p_T$  are parameterized  
 225 by the form:  $1/p_T d^2N/dp_T dy = N \cdot \exp(-(m_T - m_\Lambda)/T)$ , where  $m_T = \sqrt{(m_\Lambda^2 + p_T^2)}$  is the transverse mass,  
 226 the normalization  $N$  and the inverse slope parameter  $T$  are free parameters of the fit,  $dy$   
 227 corresponds to the measured  $y_{lab}$  range. The experimental  $\Lambda$  spectra are compared with the  
 228 predictions of the DCM-QGSM, URQMD and PHSD models. The fit results are consistent  
 229 within the uncertainties with the predictions of the models. The values of the inverse slope  $T_0$ ,  
 230 extracted from the fit of the  $p_T$  spectra, are summarized in Table 8.

231 Table 8. Inverse slope parameter extracted from the fit of the  $p_T$  spectra.

4.0 AGeV	$T_0$ , MeV (C+C)	$T_0$ , MeV (C+Al)	$T_0$ , MeV (C+Cu)	$T_0$ , MeV (C+Pb)
Experiment	95 ± 11 ± 9	119 ± 15 ± 12	125 ± 11 ± 9	130 ± 25 ± 21
$\chi^2 / \text{ndf}$	1.61/2	0.20/2	1.27/2	0.36/2
DCM-QGSM	126	120	133	130
UrQMD	107	128	133	136
PHSD	87	100	105	98



4.5 AGeV	$T_0$ , MeV (C+C)	$T_0$ , MeV (C+Al)	$T_0$ , MeV (C+Cu)	$T_0$ , MeV (C+Pb)
Experiment	$114 \pm 16 \pm 12$	$137 \pm 19 \pm 15$	$122 \pm 13 \pm 11$	$129 \pm 24 \pm 19$
$\chi^2 / \text{ndf}$	3.07/2	1.49/2	1.30/2	0.77/2
DCM-QGSM	132	133	135	142
UrQMD	122	128	130	134
PHSD	101	106	109	108

233 The systematic error of the  $\Lambda$  yield in every  $p_T$  and  $y$  bin is calculated via a quadratic sum of  
234 uncertainties coming from the following sources:

- 235 • Systematic errors of the embedding efficiency estimated by embedding the  $\Lambda$  decay  
236 products into data samples collected in different run periods.
- 237 • Systematic errors of the background subtraction under  $\Lambda$  signal in the  $(p, \pi^-)$  invariant  
238 mass spectra (see text above).
- 239 • The  $\Lambda$  yield normalization uncertainty calculated as a quadratic sum of uncertainties of  
240 the trigger efficiency, luminosity and inelastic cross section.

241 The systematic uncertainties are summarized in Tables 10 and 11.

242 Table 10. Total systematic uncertainty of the  $\Lambda$  yield for 4.0 AGeV

Target Interval	$y$				Target Interval	$p_T$			
	C sys%	Al sys%	Cu sys%	Pb sys%		C sys%	Al sys%	Cu sys%	Pb sys%
1.2-1.45	11.4	14.5	8.6	16.8	0.1-0.3	10.0	13.6	10.0	15.8
1.45-1.65	9.3	9.6	8.2	16.4	0.3-0.55	9.7	10.8	7.7	14.3
1.65-1.85	11.0	13.1	10.7	20.1	0.55-0.8	10.5	11.5	11.5	15.3
1.85-2.1	15.0	16.1	18.9	22.3	0.8-1.05	28.9	25.9	23.3	34.5
Normalization	4.9	3.8	3.0	3.0	Normalization	4.9	3.8	3.0	3.0

243 Table 11. Total systematic uncertainty of the  $\Lambda$  yield for 4.5 AGeV.

Target Interval	$y$				Target Interval	$p_T$			
	C, sys%	Al, sys%	Cu, sys%	Pb, sys%		C, sys%	Al, sys%	Cu, sys%	Pb, sys%
1.25-1.5	15.4	16.3	13.1	16.5	0.1-0.3	24.5	22.8	13.3	23.4
1.5-1.7	13.3	10.4	10.8	15.0	0.3-0.55	12.1	12.4	10.7	14.3
1.7-1.9	14.6	11.9	11.5	12.6	0.55-0.8	11.6	11.3	13.4	16.7
1.9-2.15	27.8	29.0	12.4	29.1	0.8-1.05	40.3	16.4	15.5	22.8
Normalization	4.9	3.8	3.0	3.0	Normalization	4.9	3.8	3.0	3.0

244 The integrated yields of  $\Lambda$  hyperons produced in the kinematic range of  $0.1 < p_T < 1.05$  GeV/c and  
245  $1.2 < y_{lab} < 2.1$  ( $1.25 < y_{lab} < 2.15$  for 4.5 AGeV data) in minimum bias C+C, Al, Cu, Pb interactions  
246 are summarized in Tables 12a and 12b. To extrapolate the measured yields to the full kinematic  
247 range the predictions of the DCM-QGSM and URQMD models are used. The model  
248 extrapolation factors, reconstruction efficiencies, the inverse slopes extracted from fits to the  
249 invariant  $p_T$  spectra, the estimated yields and inclusive cross sections of the  $\Lambda$  hyperon  
250 production in C+C, C+Al, C+Cu, C+Pb minimum bias interactions with beam energies of 4.0  
251 and 4.5 AGeV are also given in Tables 12a and 12b.

252 Table 12a. Extrapolation factors to the full kinematic range, reconstruction efficiencies,  $\Lambda$   
 253 hyperon yields and cross sections for 4.0 AGeV data. The first error given is statistical, the  
 254 second error is systematic.

4.0 AGeV	<b>C</b>	<b>Al</b>	<b>Cu</b>	<b>Pb</b>
DCM-QGSM URQMD extrap. factor (average)	2.76	3.08	4.23	6.17
Efficiency in $0.1 < p_T < 1.05$ GeV/c, $1.2 < y_{lab} < 2.1$	0.027	0.027	0.024	0.021
Yields in $0.1 < p_T < 1.05$ GeV/c, $1.2 < y_{lab} < 2.1$	$0.0164 \pm 0.0013 \pm 0.0010$	$0.0286 \pm 0.0025 \pm 0.0020$	$0.0307 \pm 0.0020 \pm 0.0016$	$0.0366 \pm 0.0048 \pm 0.0036$
Yields in the full kin. range $N_{part}$ DCM- QGSM	$0.0453 \pm 0.0036 \pm 0.0027$ 9	$0.0882 \pm 0.0077 \pm 0.0060$ 13.4	$0.131 \pm 0.009 \pm 0.007$ 23	$0.226 \pm 0.030 \pm 0.023$ 50.5
$\Lambda$ cross section in min. bias interact, mb	$37.6 \pm 3.0 \pm 2.3$	$111.2 \pm 9.7 \pm 7.6$	$234 \pm 16 \pm 12$	$695 \pm 91 \pm 72$
Inverse slope parameter, MeV / $\chi^2$ / ndf	$95 \pm 11 \pm 9$ 1.61/2	$119 \pm 15 \pm 12$ 0.20/2	$125 \pm 11 \pm 9$ 1.27/2	$125 \pm 25 \pm 21$ 0.36/2

255 Table 12b. Extrapolation factors to the full kinematic range, reconstruction efficiencies,  $\Lambda$   
 256 hyperon yields and cross sections for 4.5 AGeV data. The first error given is statistical, the  
 257 second error is systematic.

4.5 AGeV	<b>C</b>	<b>Al</b>	<b>Cu</b>	<b>Pb</b>
DCM-QGSM URQMD extrap. factor (average)	2.48	3.07	3.98	6.74
Efficiency in $0.1 < p_T < 1.05$ GeV/c, $1.25 < y_{lab} < 2.15$	0.020	0.021	0.016	0.014
Yields in $0.1 < p_T < 1.05$ GeV/c, $1.25 < y_{lab} < 2.15$	$0.0224 \pm 0.0026 \pm 0.0019$	$0.0355 \pm 0.0034 \pm 0.0026$	$0.0406 \pm 0.0032 \pm 0.0026$	$0.040 \pm 0.0057 \pm 0.0043$
Yields in the full kin. range $N_{part}$ DCM- QGSM	$0.0554 \pm 0.0064 \pm 0.0047$ 9	$0.109 \pm 0.010 \pm 0.008$ 13.4	$0.164 \pm 0.013 \pm 0.011$ 23	$0.273 \pm 0.038 \pm 0.029$ 50.5
$\Lambda$ cross section in min. bias interact., mb	$46.0 \pm 5.3 \pm 3.9$	$137 \pm 13 \pm 10$	$293 \pm 23 \pm 19$	$839 \pm 117 \pm 90$
Inverse slope parameter, MeV / $\chi^2$ / ndf	$114 \pm 16 \pm 12$ 3.07/2	$137 \pm 19 \pm 15$ 1.49/2	$122 \pm 13 \pm 11$ 1.30/2	$129 \pm 24 \pm 19$ 0.77/2

258 Table 12c.  $\Lambda$  hyperon yields and yields normalized to the number of nucleons-participants. The  
 259 first error is statistical, the second error is systematic. Predictions of the DCM-QGSM, UrQMD  
 260 and PHSD models are shown for carbon-carbon interactions at different beam energies.

<b>C+C</b>	<b>4.5 AGeV</b>	<b>4.0 AGeV</b>	<b>3.5 AGeV</b>	<b>2.0 AGeV</b>
BM@N yield Yield normal to $N_{part}$	0.0554±0.0064±0.0047 / 9 (6.16±0.71±0.52)·10 <sup>-3</sup>	0.0453±0.0036±0.0027 (5.03±0.40±0.30)·10 <sup>-3</sup>		
DCM-QGSM DCM-QGSM / $N_{part}$	0.1518 16.86·10 <sup>-3</sup>	0.1103 12.26·10 <sup>-3</sup>	0.0771 8.57·10 <sup>-3</sup>	0.0125 1.39·10 <sup>-3</sup>
UrQMD yield UrQMD / $N_{part}$	0.0927 10.3·10 <sup>-3</sup>	0.0736 8.17·10 <sup>-3</sup>	0.0577 6.41·10 <sup>-3</sup>	0.0118 1.31·10 <sup>-3</sup>
PHSD yield PHSD / $N_{part}$	0.1167 12.97·10 <sup>-3</sup>	0.09 10.0·10 <sup>-3</sup>	0.0684 7.6·10 <sup>-3</sup>	0.0119 1.32·10 <sup>-3</sup>
Other Experiments			(2.89±0.72) ·10 <sup>-2</sup> (3.36 AGeV) (2.8±0.3) ·10 <sup>-2</sup> (3.36 AGeV) Propane Chamber	(0.92±0.12+0.34- 0.17) ·10 <sup>-2</sup> HADES

261 Table 12d.  $\Lambda$  hyperon yields and yields normalized to the number of nucleons-participants. The  
 262 first error is statistical, the second error is systematic. Predictions of the DCM-QGSM, UrQMD  
 263 and PHSD models are shown for carbon-nucleus interactions at different beam energies.

<b>C+Al</b>	<b>4.5 AGeV</b>	<b>4.0 AGeV</b>	<b>3.5 AGeV</b>
BM@N yield Yield normal to $N_{part}$	0.109±0.010±0.008 / 13.4 (8.13±0.75±0.60)·10 <sup>-3</sup>	0.0882±0.0077±0.0060 (6.58±0.57±0.45)·10 <sup>-3</sup>	
DCM-QGSM QGSM / $N_{part}$	0.2231 16.65·10 <sup>-3</sup>	0.164 12.24·10 <sup>-3</sup>	0.1153 8.61·10 <sup>-3</sup>
UrQMD yield UrQMD / $N_{part}$	0.1414 10.55·10 <sup>-3</sup>	0.1138 8.49·10 <sup>-3</sup>	0.092 6.86·10 <sup>-3</sup>
PHSD yield PHSD / $N_{part}$	0.1685 12.58·10 <sup>-3</sup>	0.1339 9.99·10 <sup>-3</sup>	0.0983 7.34·10 <sup>-3</sup>
<b>C+Cu</b>	<b>4.5 AGeV</b>	<b>4.0 AGeV</b>	<b>3.5 AGeV</b>
BM@N yield Yield normal to $N_{part}$	0.164±0.013±0.011 / 23 (7.13±0.56±0.48)·10 <sup>-3</sup>	0.131±0.009±0.007 (5.70±0.39±0.30)·10 <sup>-3</sup>	
DCM-QGSM QGSM / $N_{part}$	0.3279 14.26·10 <sup>-3</sup>	0.2503 10.88·10 <sup>-3</sup>	0.1782 7.75·10 <sup>-3</sup>
UrQMD yield UrQMD / $N_{part}$	0.2108 9.16·10 <sup>-3</sup>	0.1732 7.53·10 <sup>-3</sup>	0.1367 5.94·10 <sup>-3</sup>
PHSD yield PHSD / $N_{part}$	0.2433 10.58·10 <sup>-3</sup>	0.1914 8.32·10 <sup>-3</sup>	0.1445 6.28·10 <sup>-3</sup>
<b>C+Pb</b>	<b>4.5 AGeV</b>	<b>4.0 AGeV</b>	<b>3.5 AGeV</b>
BM@N yield Yield normal to $N_{part}$	0.273±0.038±0.029 / 50.5 (5.41±0.75±0.57)·10 <sup>-3</sup>	0.226±0.030±0.023 (4.48±0.59±0.46)·10 <sup>-3</sup>	
DCM-QGSM QGSM / $N_{part}$	0.4937 9.78·10 <sup>-3</sup>	0.3872 7.67·10 <sup>-3</sup>	0.277 5.48·10 <sup>-3</sup>
UrQMD yield UrQMD / $N_{part}$	0.3504 6.94·10 <sup>-3</sup>	0.2947 5.84·10 <sup>-3</sup>	0.2215 4.39·10 <sup>-3</sup>
PHSD yield	0.3798	0.3033	0.2261

PHSD / $N_{part}$	$7.52 \cdot 10^{-3}$	$6.01 \cdot 10^{-3}$	$4.48 \cdot 10^{-3}$
-------------------	----------------------	----------------------	----------------------

264 In general, the transport models describe the shape of the differential spectra on  $y^*$  and  $p_T$ , but  
265 predict more abundant yields of  $\Lambda$  hyperons than measured in the experiment. The UrQMD  
266 model predictions are closer to the experimental data in the normalization than the predictions of  
267 the DCM-QGSM and PHSD models. The PHSD model predicts a stronger rise of the  $\Lambda$  hyperon  
268 yields in the BM@N kinematic range with the atomic weight of the target than the DCM-QGSM  
269 and UrQMD models. This tendency is deduced from the rapidity spectra of  $\Lambda$  hyperons generated  
270 in the models which are shown in Fig.12e.

271 The  $\Lambda$  yields and production cross sections in  $C+C$  interactions can be compared with the  
272 previous results of  $23.2 \pm 2.5$  mb [ArmutCC] and  $24 \pm 6$  mb [ArakelianCC] measured in  
273 interactions of the carbon beam with the momentum of 4.2 GeV/c per nucleon (beam kinetic  
274 energy of 3.36 GeV per nucleon) with the Propane Chamber experiment, as well as with the  
275 result of the HADES experiment at 2A GeV. In Fig.16a the BM@N result for the  $\Lambda$  yield in  $C+C$   
276 minimum bias interactions is compared with the results taken from other experiments  
277 [ArakelianCC], [ArmutCC], [HadesL0]. The  $C+C$  data are compared with predictions of the  
278 DCM-QGSM, UrQMD and PHSD transport models (Fig16a and Table 12c). There is a general  
279 tendency that the transport models predict a faster rise of the  $\Lambda$  hyperon yield with the energy in  
280 comparison with the experimental data. The energy dependences of the  $\Lambda$  yields measured in  
281 BM@N are also presented in Table 12d and Fig.16b,c,d for  $C+Al$ ,  $C+Cu$ ,  $C+Pb$  minimum bias  
282 interactions, respectively. The predictions of the transport models are shown. In general, the  
283 model predictions exceed the experimental data in the normalization. The DCM-QGSM model  
284 predicts a higher full yield of  $\Lambda$  hyperons than the two other models.

285 Table 13. Yields and inclusive cross sections of  $\Lambda$  hyperon production in interactions of light and  
286 medium nucleus.

Interacting nucleus / reference	Beam momentum, kinetic energy ( $E_{kin}$ )	$\Lambda$ cross section, mb	$\Lambda$ yield, $\cdot 10^{-2}$
$He_4+Li_6$	4.5 GeV/c (3.66A GeV)	$5.9 \pm 1.5$	$1.85 \pm 0.5$
$C+C$	4.2 GeV/c (3.36A GeV)	$24 \pm 4$	$2.89 \pm 0.72$
$C+C$ , propane Chamber	4.2 GeV/c (3.36A GeV)	$23.2 \pm 2.5$	$2.8 \pm 0.3$
$p+p$	4.95 GeV/c (4.1 GeV)		$2.3 \pm 0.4$
$C+C$ , HADES	2A GeV	$8.7 \pm 1.1 \pm^{3.2}_{1.6}$	$0.92 \pm 0.12 \pm^{0.34}_{0.17}$
$Ar+KCl$ , HADES	1.76A GeV		$3.93 \pm 0.14 \pm 0.15$
$Ar+KCl$ , FOPI	1.93A GeV		$3.9 \pm 0.14 \pm 0.08$
$Ni+Ni$ , FOPI, central 390 mb from 3.1 $b$	1.93A GeV		$0.137 \pm 0.005 \pm^{0.009}_{0.025}$
$Ni+Cu$ , EOS, full $b < 8.9$ fm / central $b < 2.4$ fm	2A GeV	$112 \pm 24 / 20 \pm 3$	
$Ar+KCl$ , central	1.8A GeV	$7.6 \pm 2.2$	

287 To compare yields of particle production in nucleus-nucleus interactions, they are usually  
 288 normalized to the mean number of nucleons participating in interactions (Participants). The  
 289 numbers of Participants in minimum bias  $C+C$ ,  $C+Al$ ,  $C+Cu$ ,  $C+Pb$  interactions are estimated  
 290 using the DCM-QGSM model [GenisPart]. The results ( $A_1+A_2$ ) are shown in Table 14. The  
 291 ratios of the  $\Lambda$  hyperon yields to the number of nucleons-participants measured in BM@N  
 292 carbon-nucleus interactions are presented in Fig.17 and in Tables 12c,d. The ratios reach  
 293 maximal values of  $0.62 \cdot 10^{-2}$  and  $0.76 \cdot 10^{-2}$  for  $C+Al$  interactions at 4.0 and 4.5 AGeV,  
 294 respectively. There is a tendency that the measured ratios are smoothly decreasing for heavier  
 295 target nuclei. This tendency is also reproduced by the transport model predictions shown in  
 296 Fig.17.

297 Table 14. Number of Participants in minimum bias  $A+A$  events at 4A GeV.

$A_1 A_2$	$A_1$	$A_2$	$A_1 + A_2$
$C+C$	4.5	4.5	9.0
$C+Al$	5.23	8.14	13.37
$C+Cu$	6.21	16.79	23.0
$C+Pb$	7.33	43.15	50.48

## 298 Summary

299 Production of  $\Lambda$  hyperons in interactions of the carbon beam with  $C$ ,  $Al$ ,  $Cu$ ,  $Pb$  targets was  
 300 studied with the BM@N detector. The analysis procedure is described including details of the  $\Lambda$   
 301 hyperon reconstruction, efficiency and systematic uncertainty evaluation. First physics results  
 302 are presented on  $\Lambda$  hyperon yield and cross sections in minimum bias carbon-nucleus interactions  
 303 at the beam kinetic energies of 4.0 and 4.5 AGeV. The results are compared with models of  
 304 nucleus-nucleus interactions and with the results of other experiments studied carbon-nucleus  
 305 interactions at lower energies.

## 306 Bibliography

- 307 [DeuteronPaper] D.Baranov et al., First Results from BM@N Technical Run with Deuteron  
 308 Beam, Phys. Part. Nucl. Lett. 15, no. 2, 148 (2018)  
 309 [GEMconf] [http://bmshift.jinr.ru/wiki/lib/exe/detail.php?id=run\\_5\\_december\\_2016&media=setting\\_1\\_f.jpg](http://bmshift.jinr.ru/wiki/lib/exe/detail.php?id=run_5_december_2016&media=setting_1_f.jpg)  
 310 [GEMTDR] [http://bmshift.jinr.ru/wiki/lib/exe/fetch.php?media=tdr\\_gem\\_may2017\\_v1.doc](http://bmshift.jinr.ru/wiki/lib/exe/fetch.php?media=tdr_gem_may2017_v1.doc)  
 311 [CBM1] V. Akishina and I. Kisel. Time-based cellular automaton track finder for the CBM  
 312 experiment - 2015. J. Phys.: Conf. Ser. 599, 012024  
 313 [CBM2] S. Gorbunov and I. Kisel. Reconstruction of decayed particles based on the Kalman  
 314 filter - 2007. CBM-SOFTnote--003  
 315 [GenisPart] Result of Genis Musulmanbekov, private communication  
 316 [AnikinaCC] N.Anikina et al., Z.Phys.C, 25,(1984),1  
 317 [ArmutCC] D.Armutiljsky et al., P1-85-220, JINR, Dubna  
 318 [ArakelianCC] S.Arakelian et al., P1-83-354, JINR, Dubna  
 319 [AngelovCC] H.Angelov et al., P1-80-473, JINR, Dubna  
 320 [HadesL0] Kalliopi Kanaki, PhD "Study of  $\Lambda$  hyperon production  
 321 in  $C+C$  collisions at 2A GeV beam energy with the HADES spectrometer", 2007  
 322

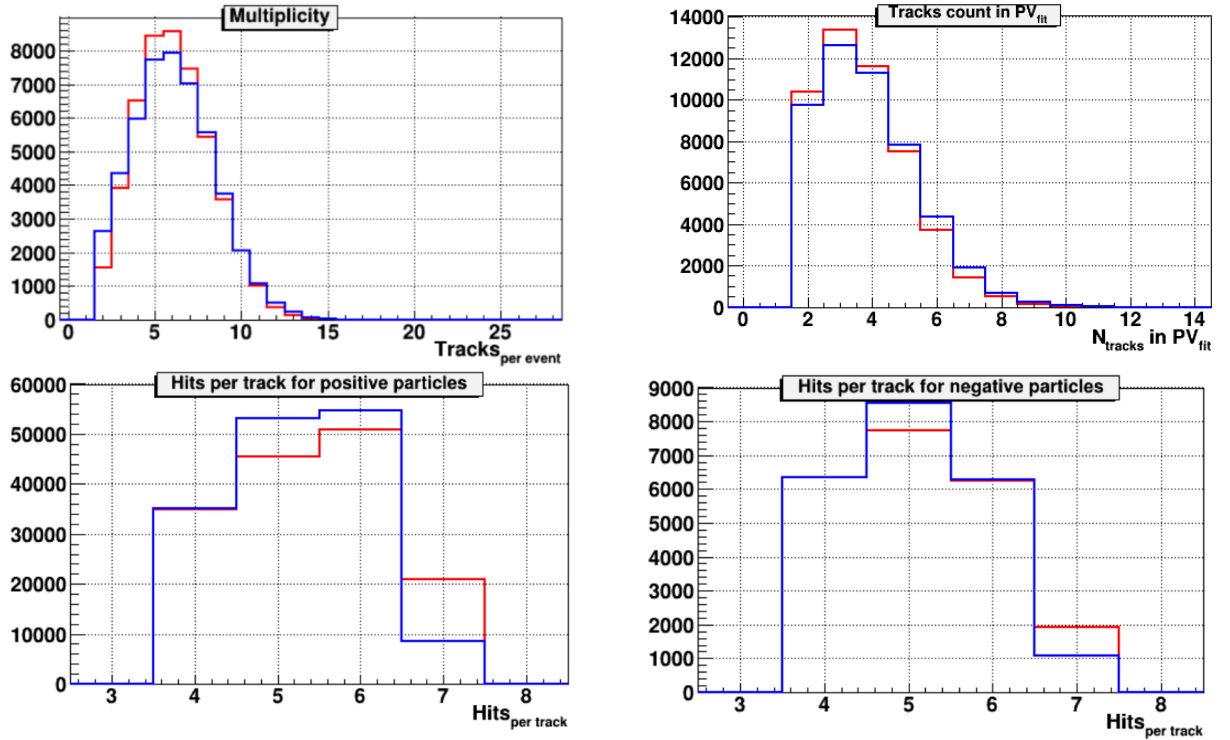


Fig.2a.  $C+Cu$  interactions at 4.0 AGeV carbon beam energy: comparison of experimental distributions (red lines) and Monte Carlo GEANT distributions of events generated with the DCM-QGSM model (blue lines): track multiplicity per event; number of tracks reconstructed in the primary vertex; number of hits per positive particle reconstructed in 1 Si + 6 GEM detectors; number of hits per negative particle.

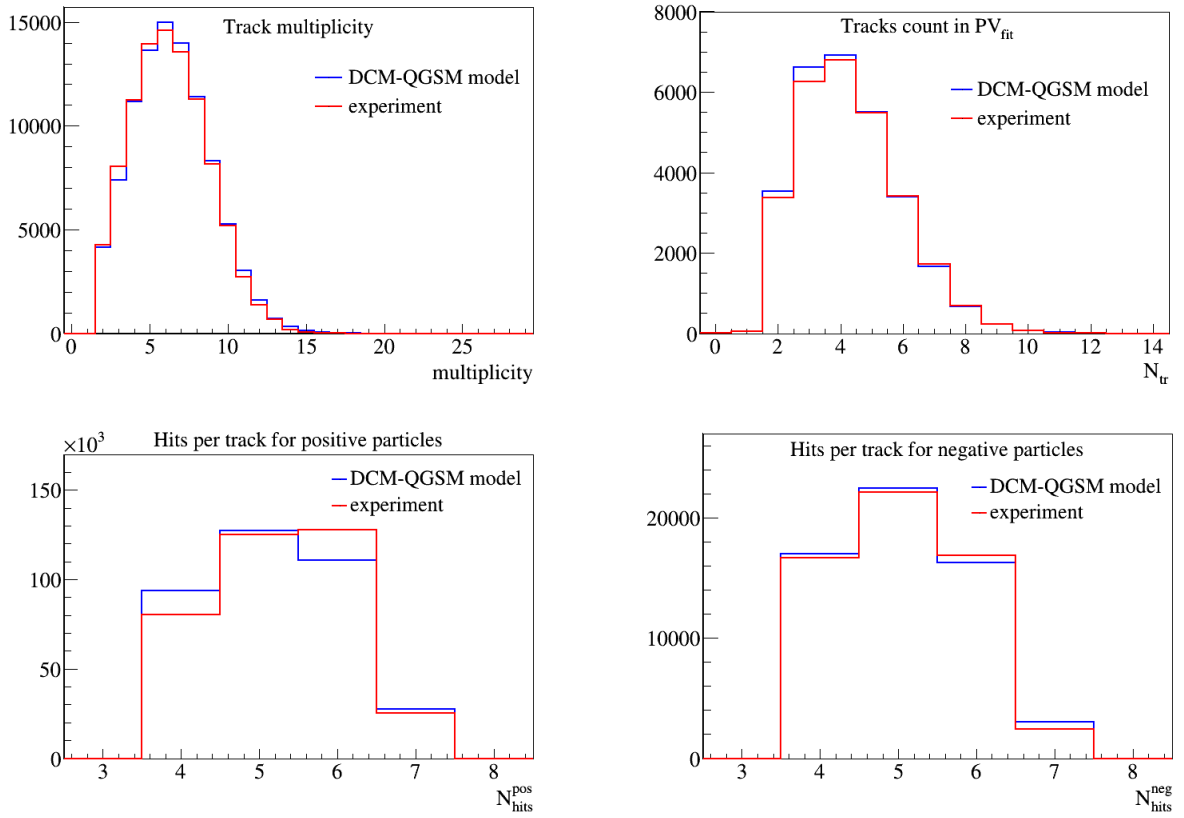


Fig.2b.  $C+Cu$  interactions at 4.5 AGeV carbon beam energy: comparison of experimental distributions (red lines) and Monte Carlo GEANT distributions of events generated with the DCM-QGSM model (blue lines): track multiplicity per event; number of tracks reconstructed in the primary vertex; number of hits per positive particle reconstructed in 1 Si + 6 GEM detectors; number of hits per negative particle.

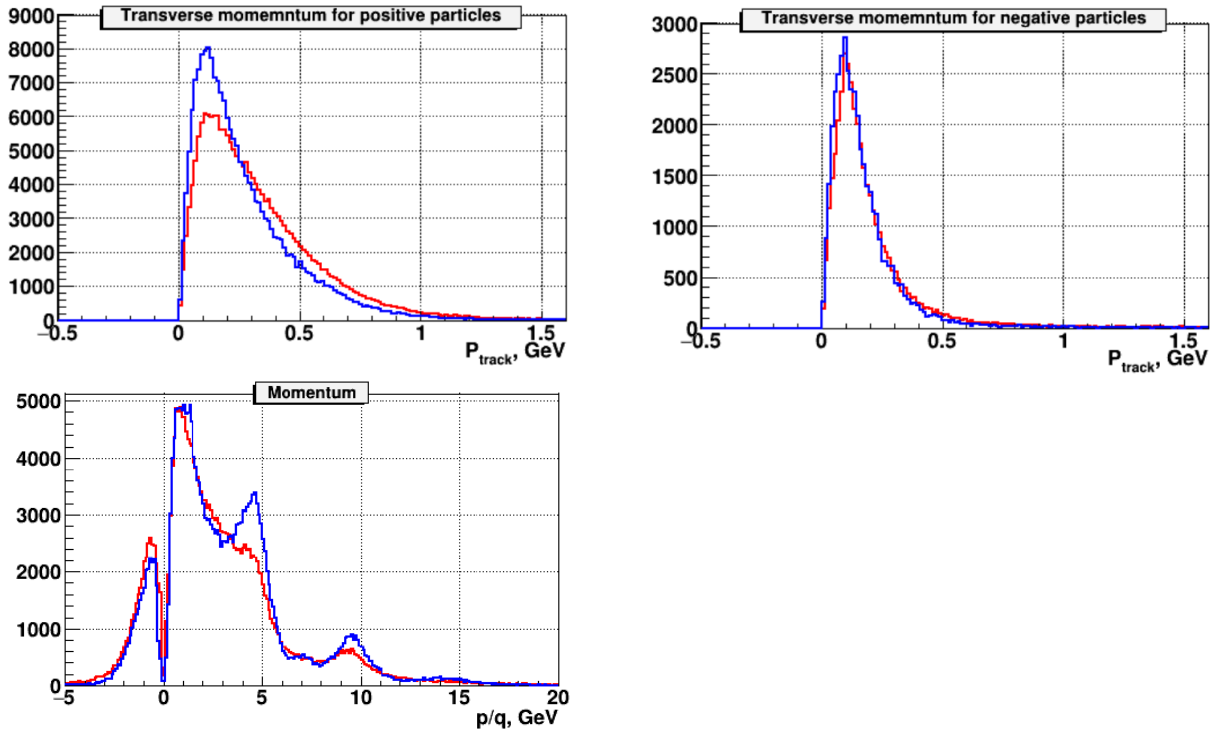
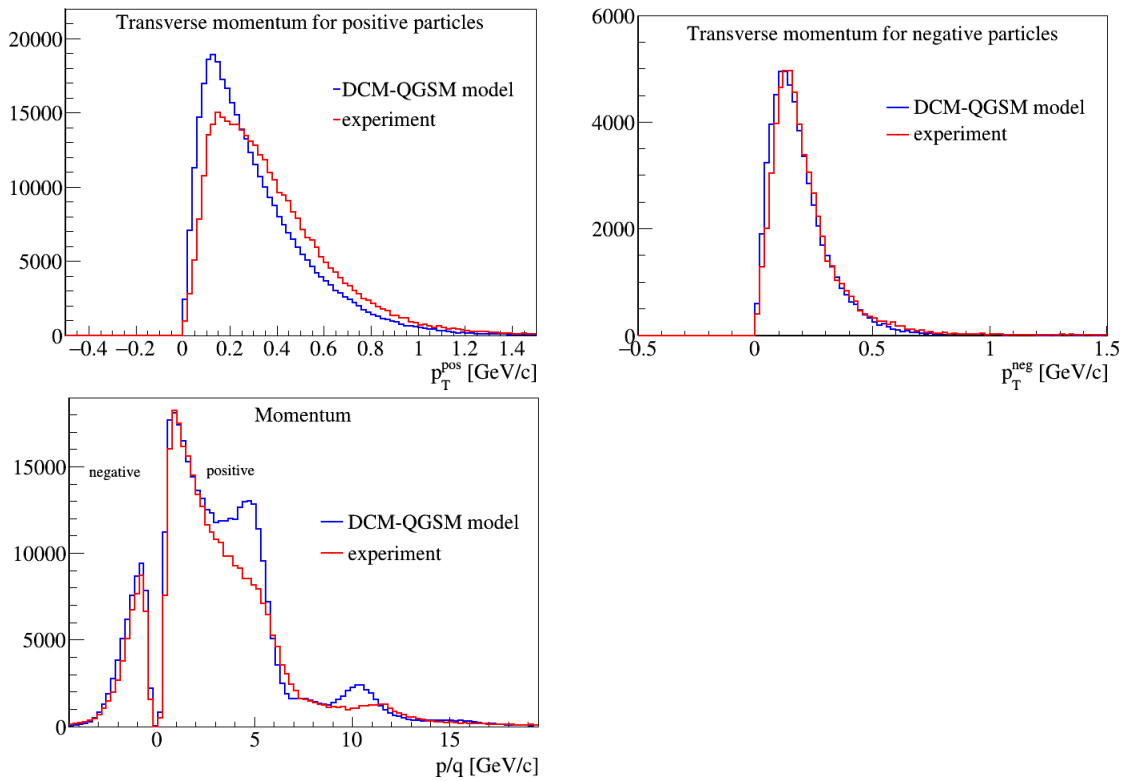


Fig. 3a.  $C+Cu$  interactions at 4.0 AGeV carbon beam energy: comparison of experimental data (red curves) and DCM-QGSM + GEANT Monte Carlo simulation (blue curves): transverse momentum of positive particles; transverse momentum of negative particles; total momentum of negative ( $p/q < 0$ ) and positive particles ( $p/q > 0$ ).

323



324

Fig. 3b.  $C+Cu$  interactions at 4.5 AGeV carbon beam energy: comparison of experimental data (red curves) and DCM-QGSM + GEANT Monte Carlo simulation (blue curves): transverse momentum of positive particles; transverse momentum of negative particles; total momentum of negative ( $p/q < 0$ ) and positive particles ( $p/q > 0$ ).

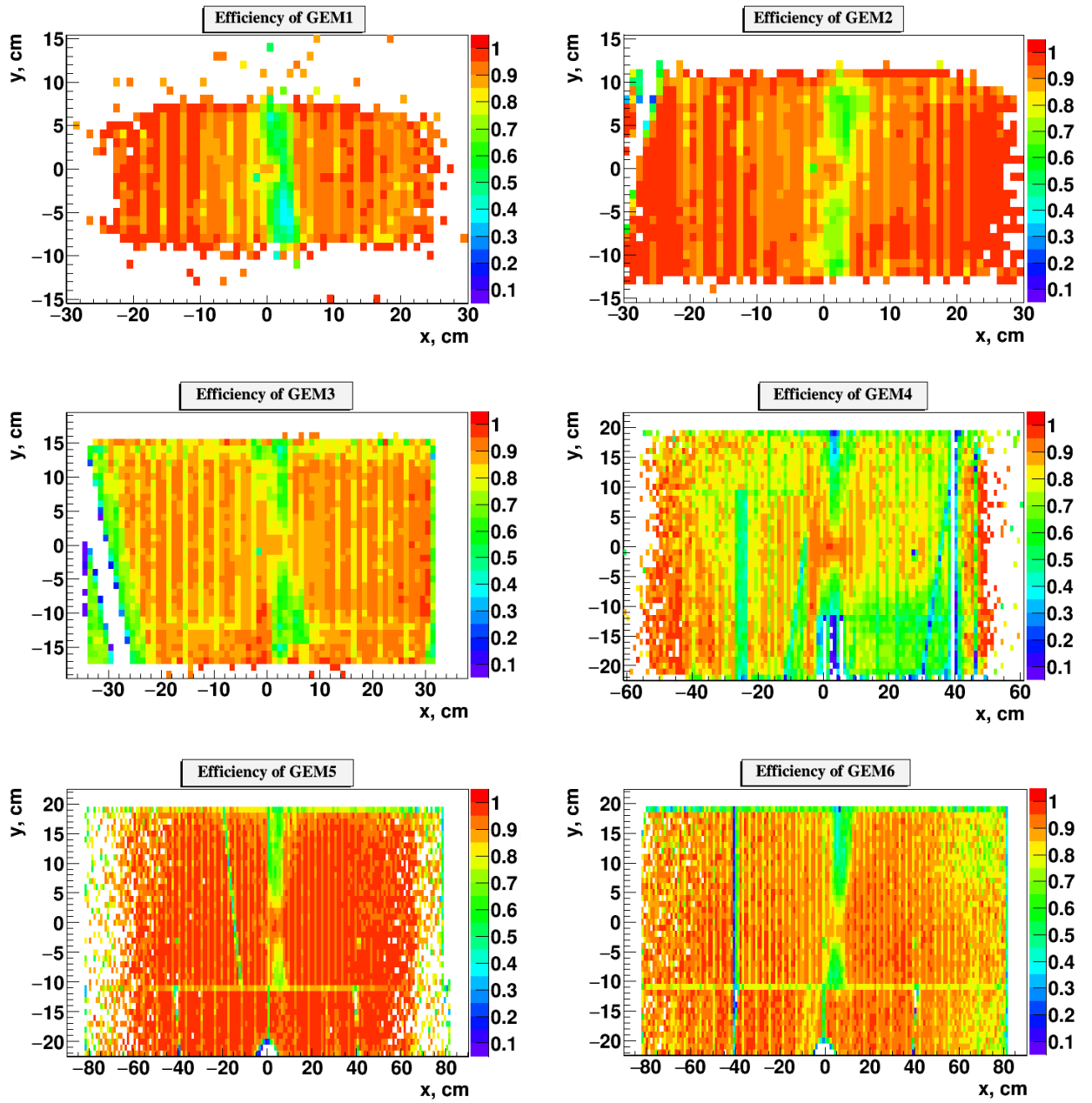


Fig. 4. Two-dimensional  $X/Y$  efficiency distributions in 6 GEM stations measured with experimental tracks and implemented into Monte Carlo simulation.

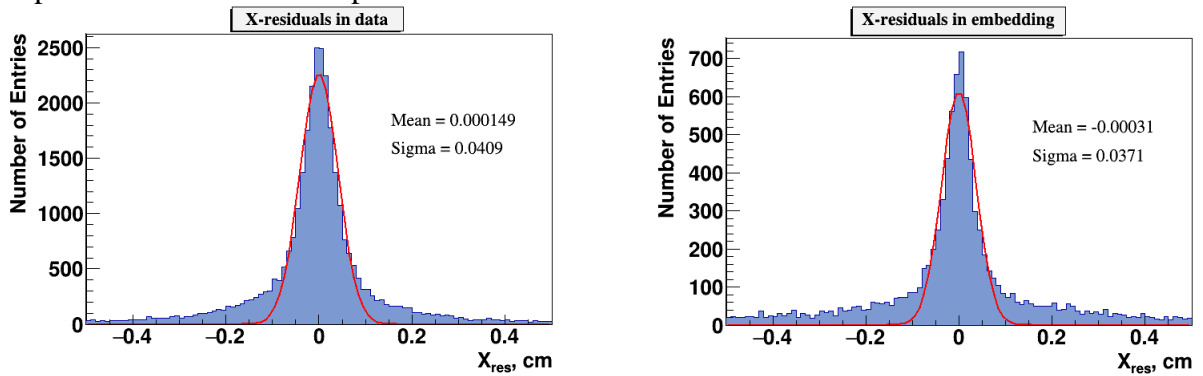


Fig. 5. Residual distributions of GEM hits with respect to reconstructed tracks: left) experimental data, right) reconstructed tracks of embedded  $\Lambda$  decay products.



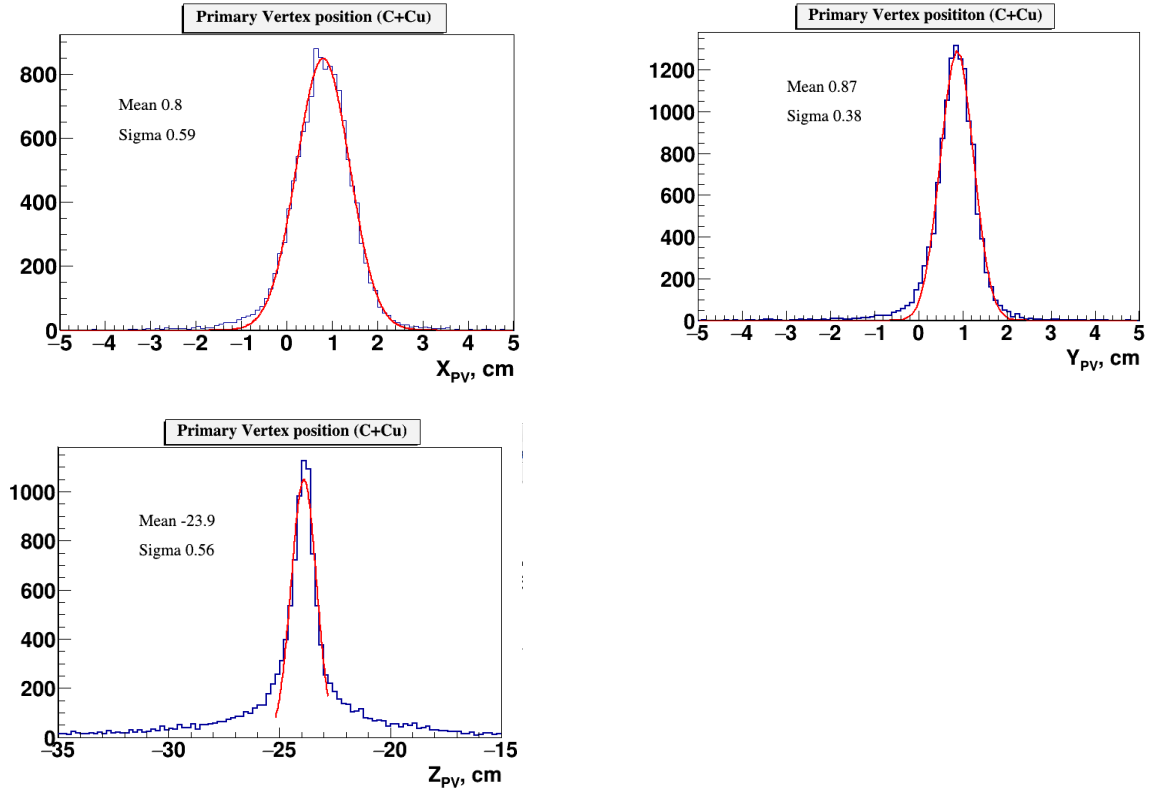


Fig. 6. X,Y,Z distributions of the experimental primary vertex.

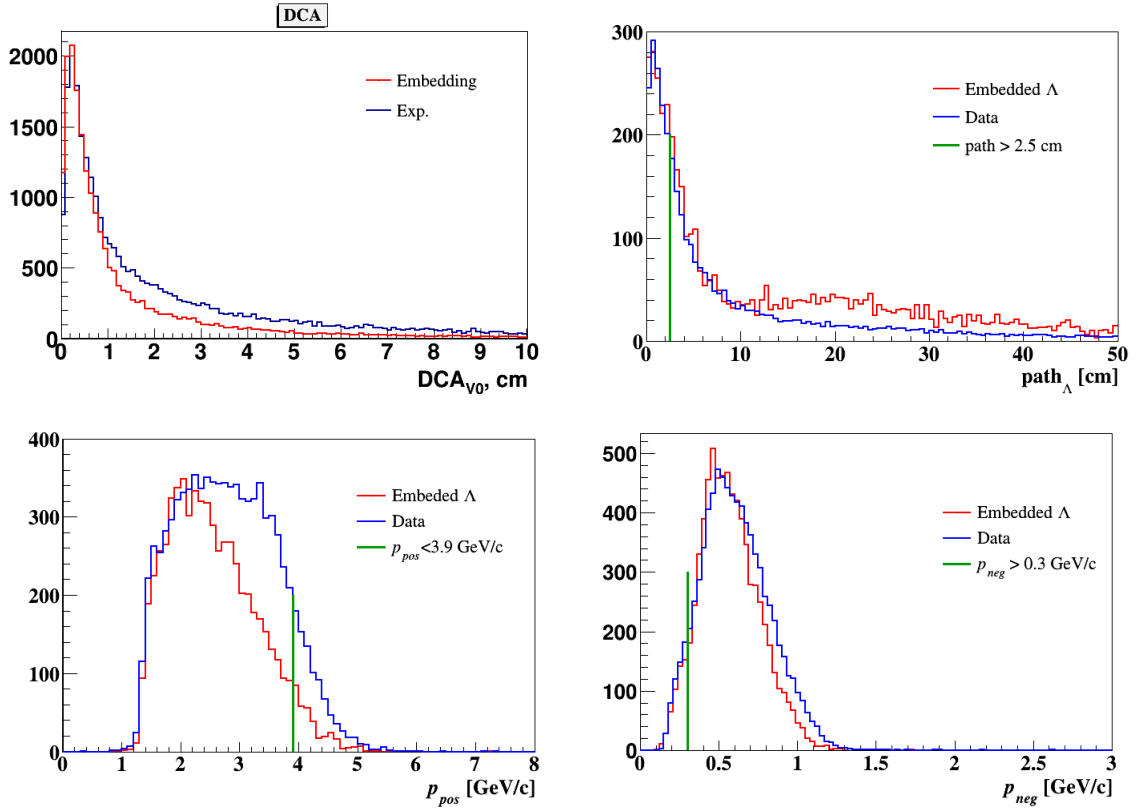


Fig.7. Distance of the closest approach of  $V0$  decay tracks ( $dca$ ), distance between the primary vertex and  $V0$  (path), momentum distributions of positive, negative tracks from  $V0$  decays. Experimental data at 4.0 AGeV carbon beam energy are compared with distributions for embedded  $\Lambda$  hyperons.

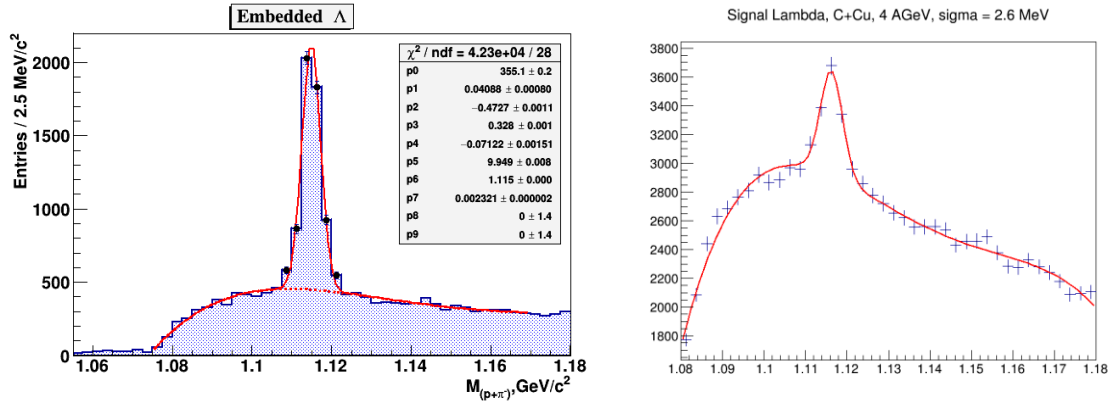


Fig. 8. The invariant mass spectrum of  $(p, \pi^-)$  pairs reconstructed in the experimental events of  $C+Cu$  interactions at 4.0 AGeV carbon beam energy with embedded  $\Lambda$  hyperon decay products (left); The invariant mass spectrum of  $(p, \pi^-)$  pairs reconstructed in  $C+Cu$  interactions (right).

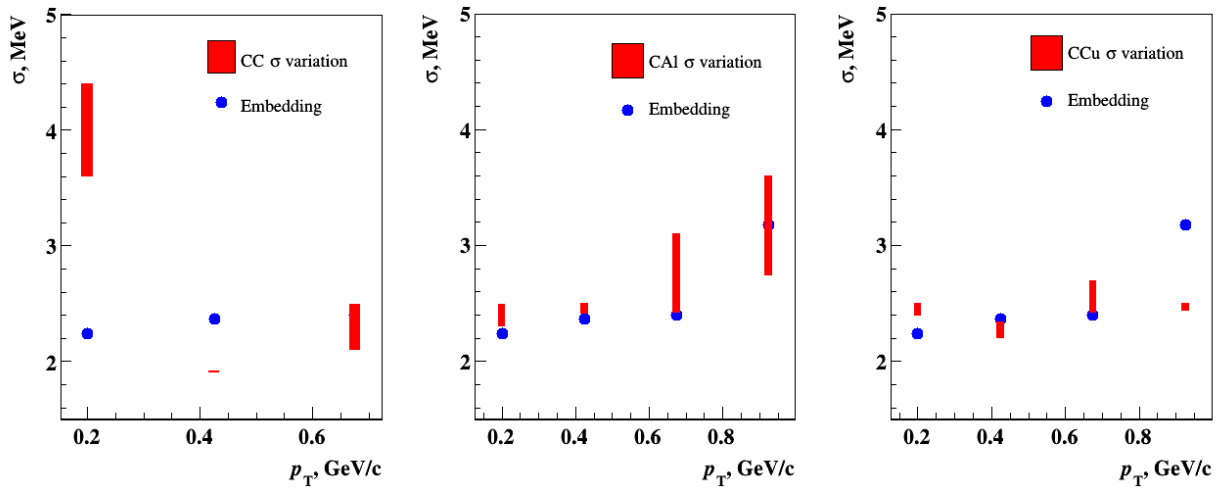
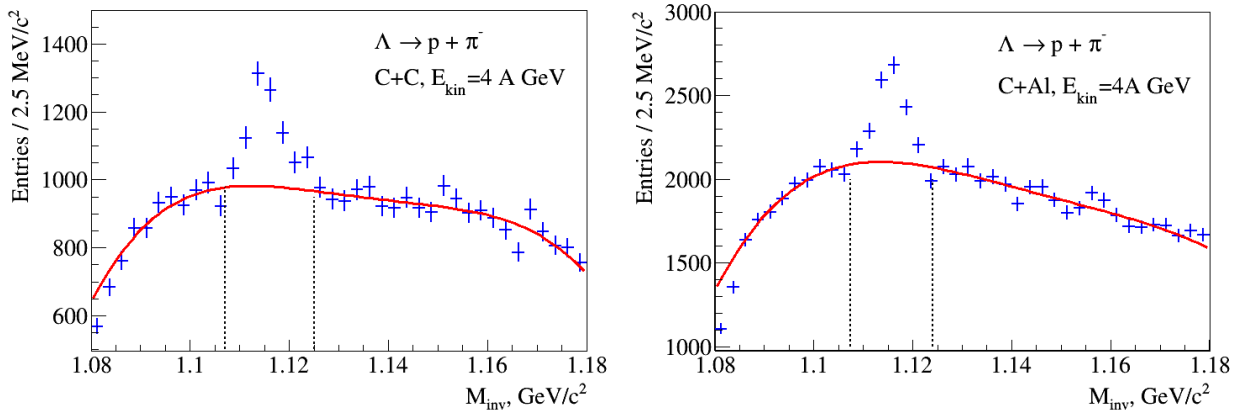


Fig.9. Variation of sigma of the experimental  $\Lambda$  and embedded  $\Lambda$  signals reconstructed in bins of  $p_T$  in  $C+C$ ,  $C+Al$ ,  $C+Cu$  interactions at 4.0 AGeV carbon beam energy. To estimate statistical fluctuations of the experimental  $\Lambda$  signal, the Gaussian fit is performed for the mass distribution shifted at a half of the mass bin ( $1.25 \text{ MeV}/c^2$ ). The differences in sigma are presented as error bands.



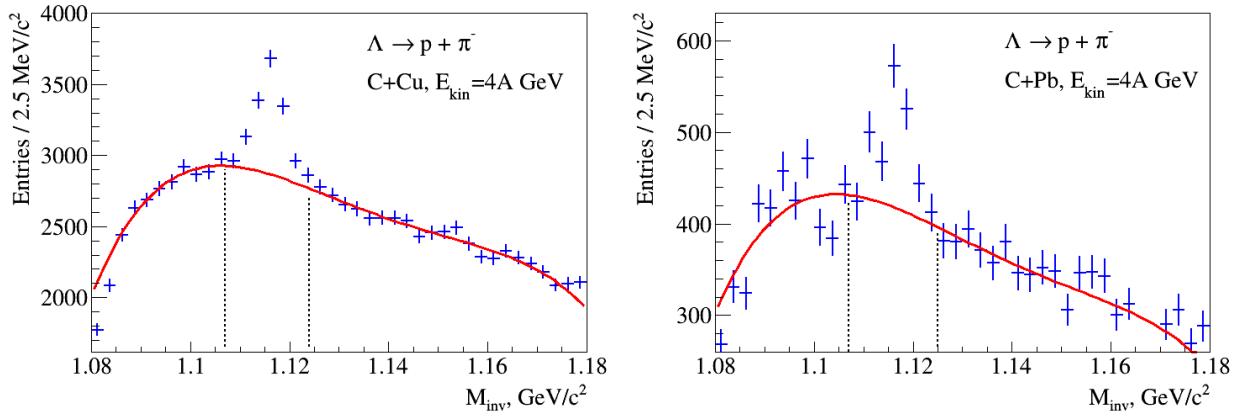


Fig. 10a.  $\Lambda \rightarrow p\pi^-$  signal reconstructed in  $C+C$ ,  $Al$ ,  $Cu$ ,  $Pb$  interactions at 4.0 AGeV carbon beam energy. The background is fitted by the 4<sup>th</sup> degree Legendre polynomial and subtracted from the histogram content in the  $\Lambda$  signal mass range indicated by the vertical lines.

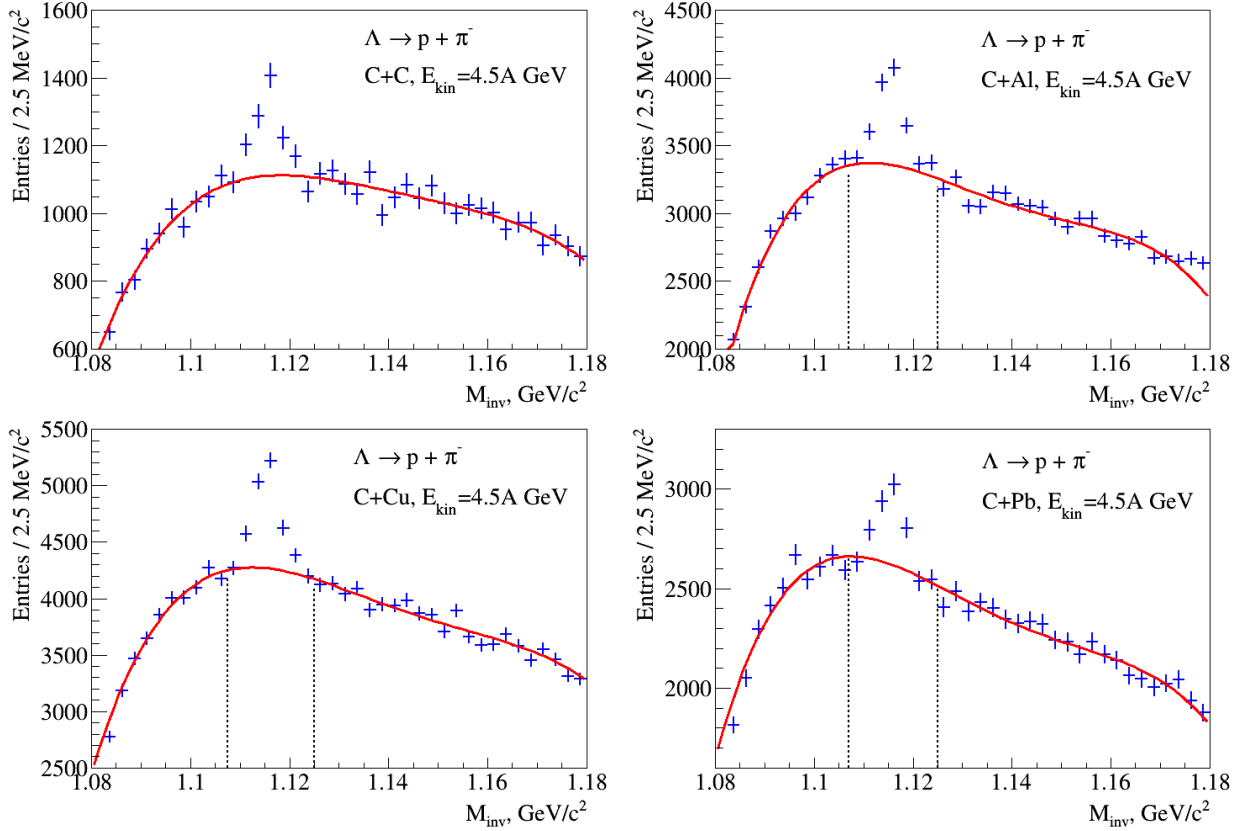
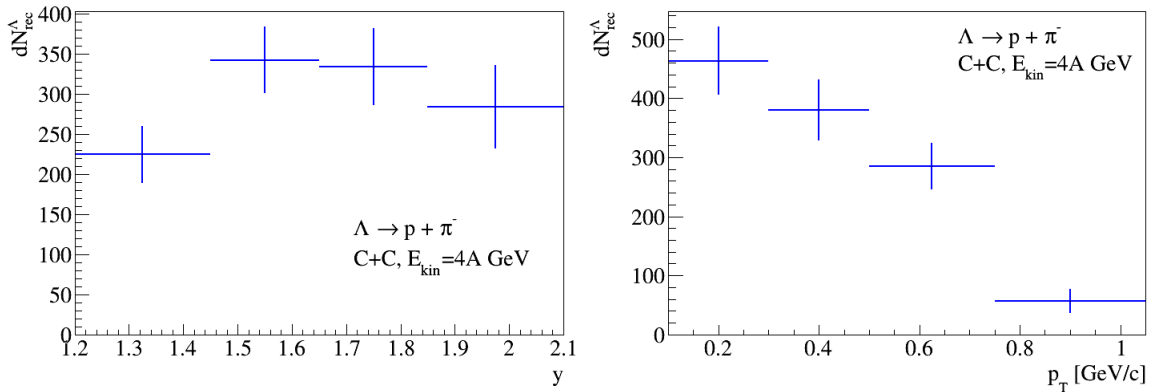


Fig. 10b.  $\Lambda \rightarrow p\pi^-$  signal reconstructed in  $C+C$ ,  $Al$ ,  $Cu$ ,  $Pb$  interactions at 4.5 AGeV carbon beam energy. The background is fitted by the 4<sup>th</sup> degree Legendre polynomial and subtracted from the histogram content in the  $\Lambda$  signal mass range indicated by the vertical lines.



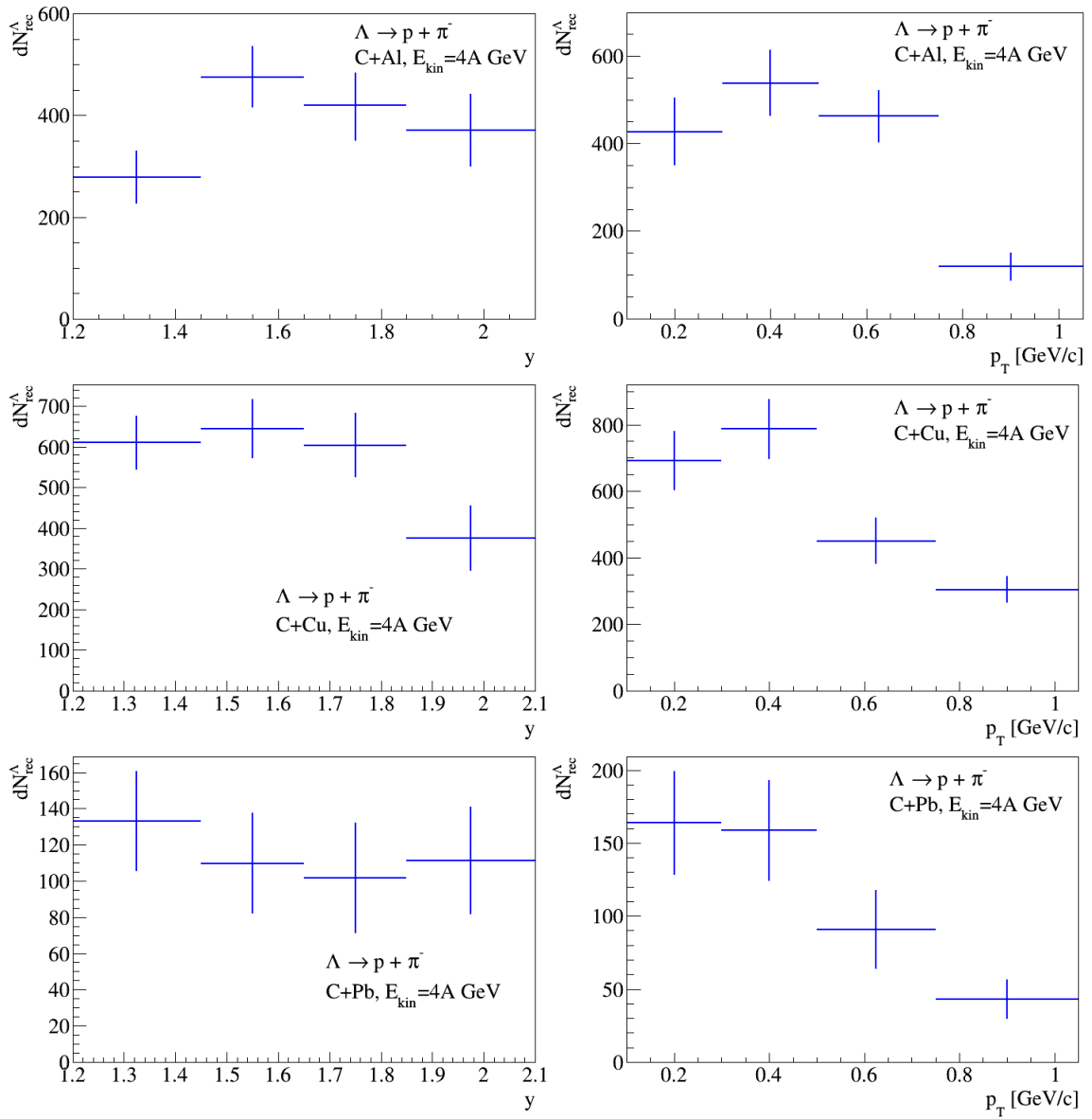
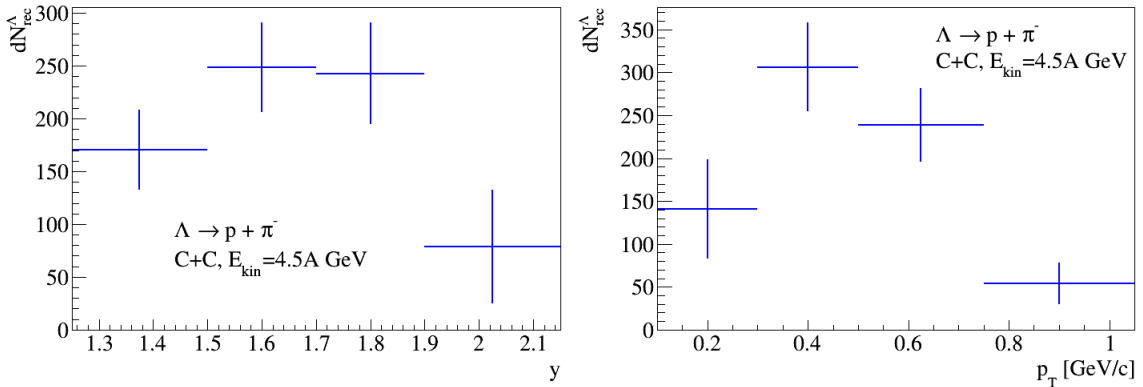


Fig.11a. Number of reconstructed  $\Lambda$  hyperons in interaction of 4.0 AGeV carbon beam with C, Al, Cu, Pb targets in bins of  $y_{lab}$  and  $p_T$ .



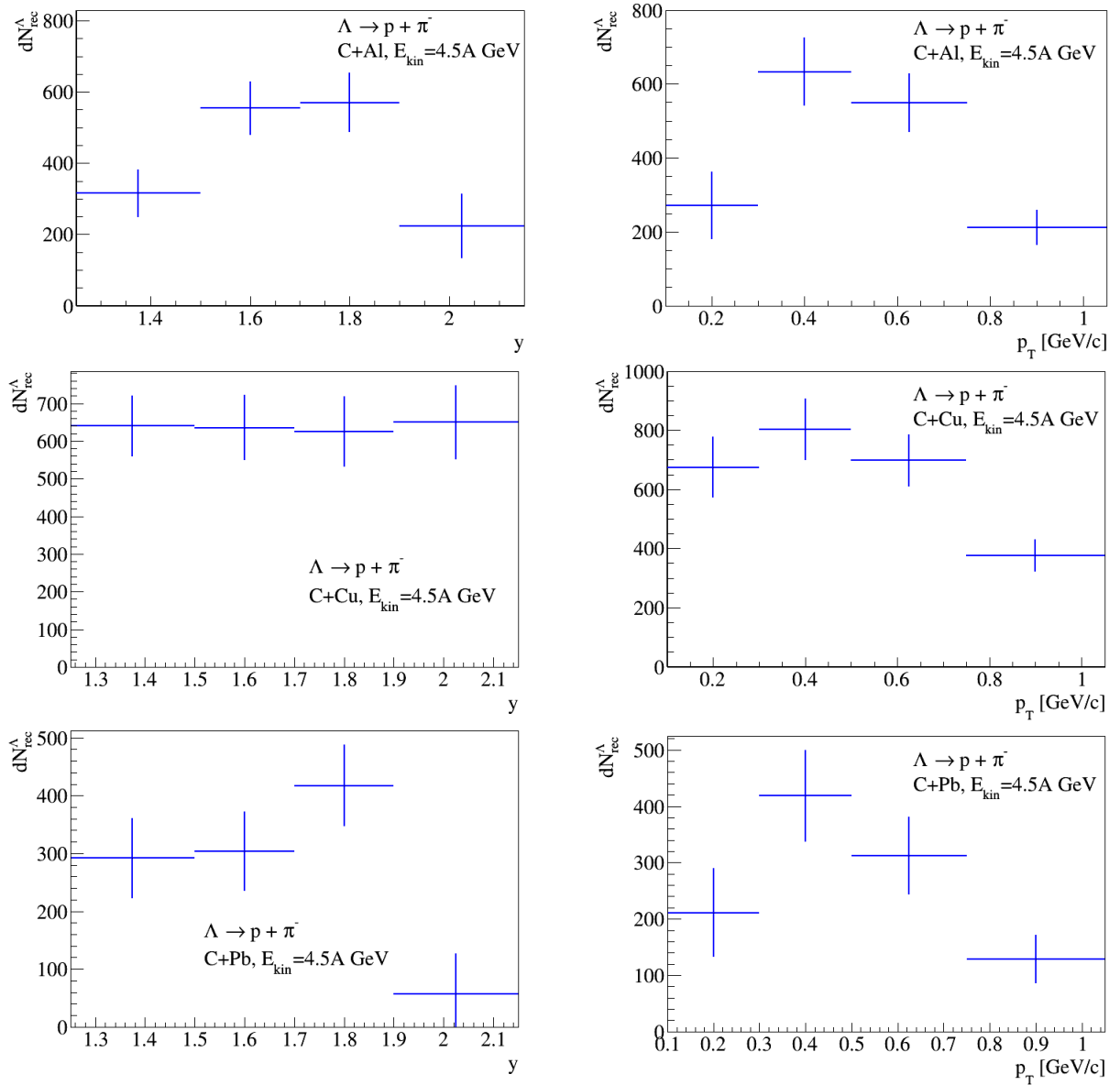
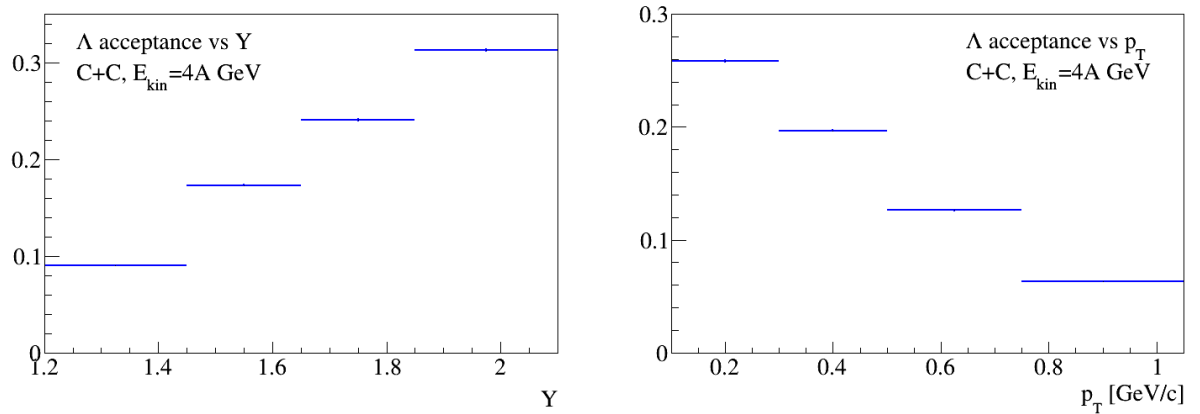


Fig.11b. Number of reconstructed  $\Lambda$  hyperons in interaction of 4.5 AGeV carbon beam with C, Al, Cu, Pb targets in bins of  $y_{lab}$  and  $p_T$ .



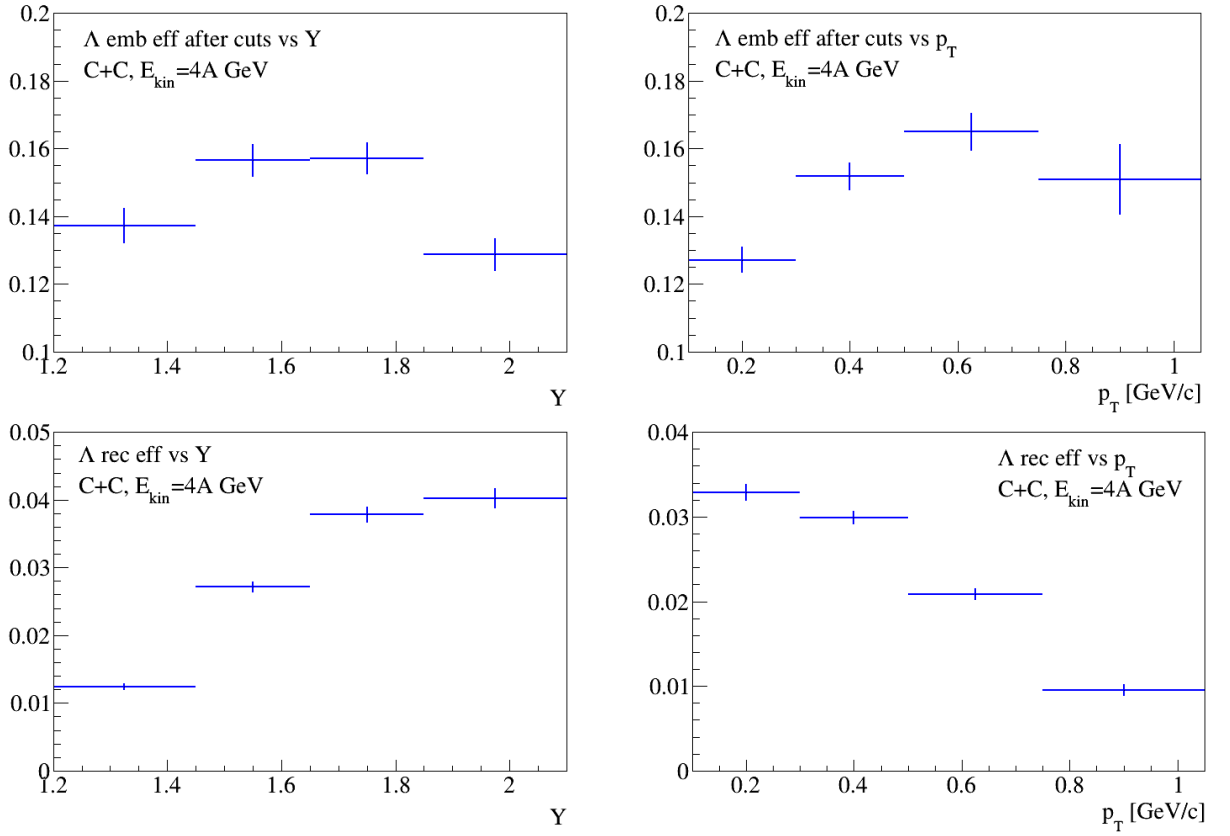
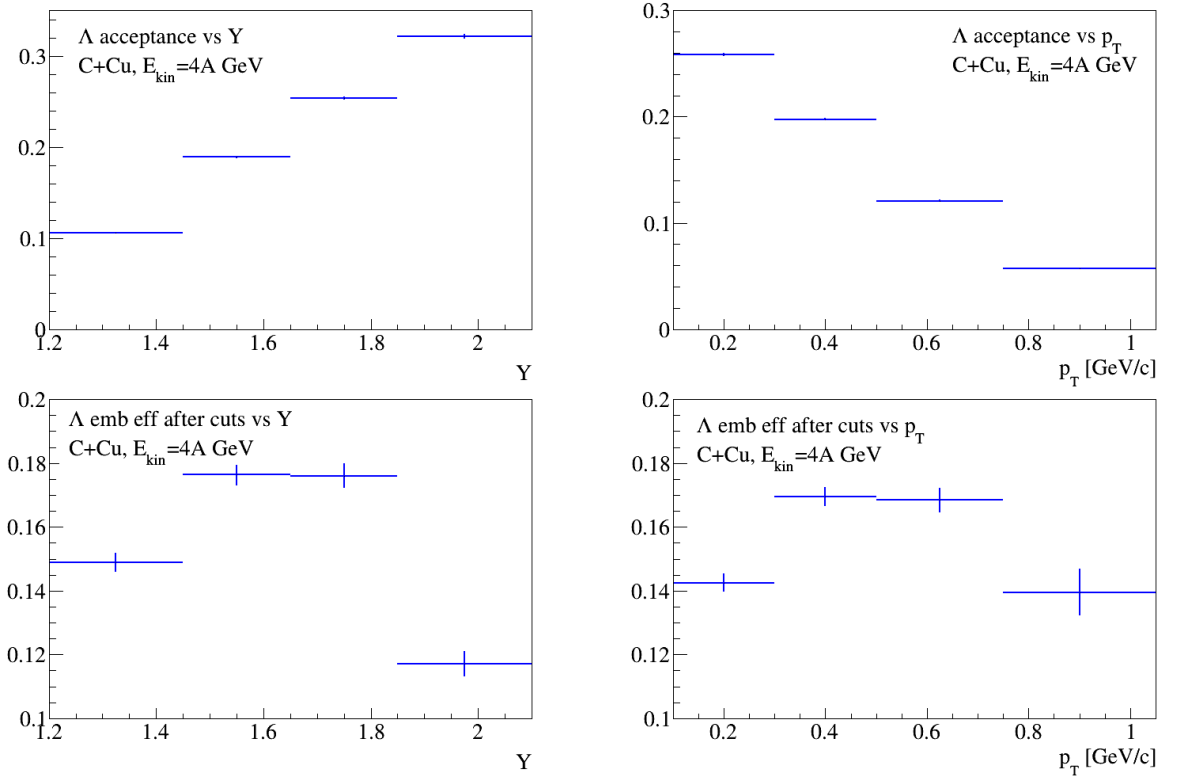


Fig.12a.  $\Lambda$  geometrical acceptance ( $\epsilon_{acc}$ ); efficiency of reconstruction of embedded  $\Lambda$  after applying kinematic and spatial cuts ( $\epsilon_{emb+cuts}$ ) and full reconstruction efficiency ( $\epsilon_{rec}$ ) shown in bins of rapidity  $y_{lab}$  in the laboratory frame (left plots) and in bins of  $p_T$  (right plots). Results are shown for C+C interactions at 4.0 AGeV carbon beam energy.



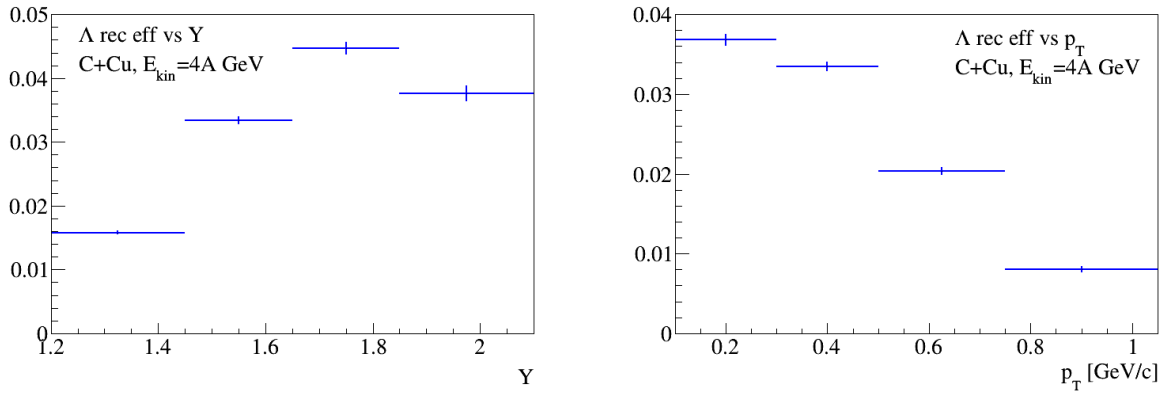


Fig.12b.  $\Lambda$  geometrical acceptance ( $\varepsilon_{acc}$ ), efficiency of reconstruction of embedded  $\Lambda$  after applying kinematic and spatial cuts ( $\varepsilon_{emb+cuts}$ ) and full reconstruction efficiency ( $\varepsilon_{rec}$ ) shown in bins of rapidity  $y_{lab}$  in the laboratory frame (left plots) and in bins of  $p_T$  (right plots). Results are shown for  $C+Cu$  interactions at 4.0 AGeV carbon beam energy.

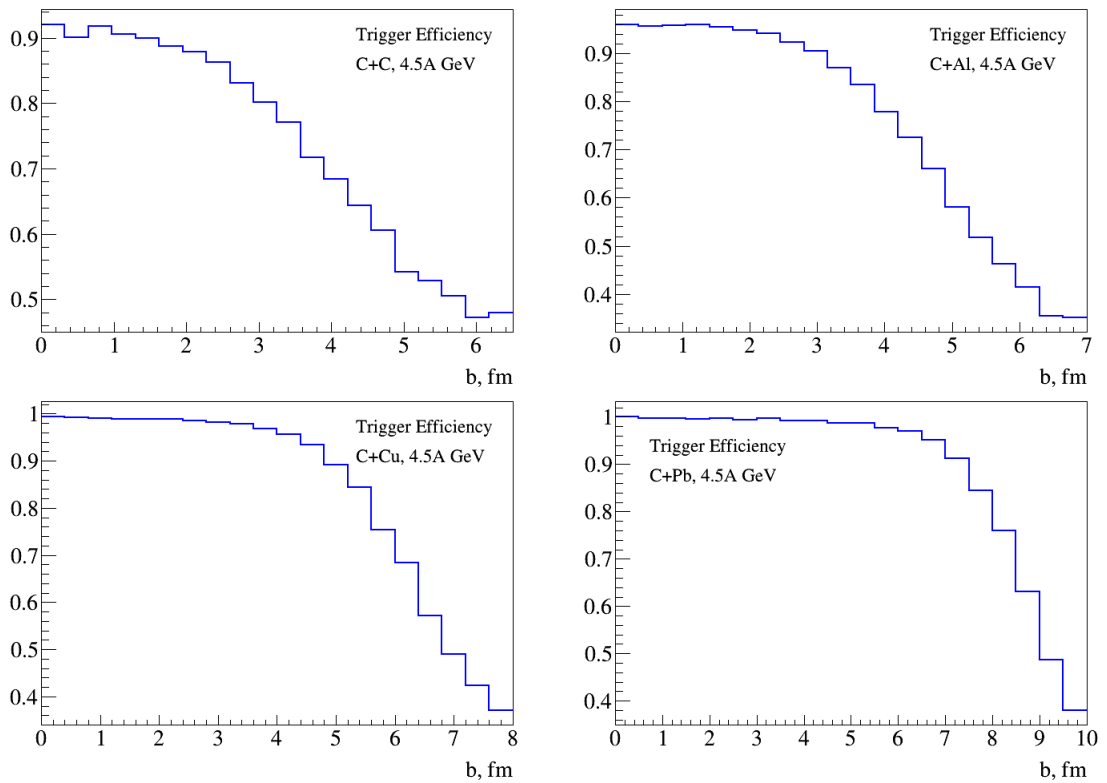
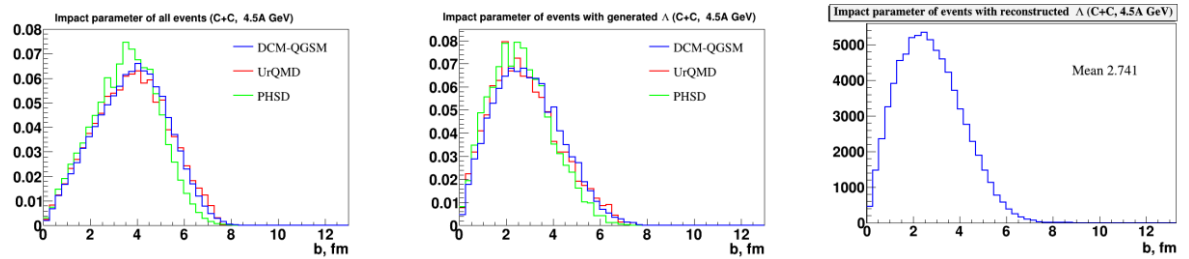


Fig.12c. Trigger efficiency ( $\varepsilon_{trig}$ ) calculated for DCM-QGSM interactions of the carbon beam with the  $C$ ,  $Al$ ,  $Cu$ ,  $Pb$  targets shown as a function of the collision impact parameter.



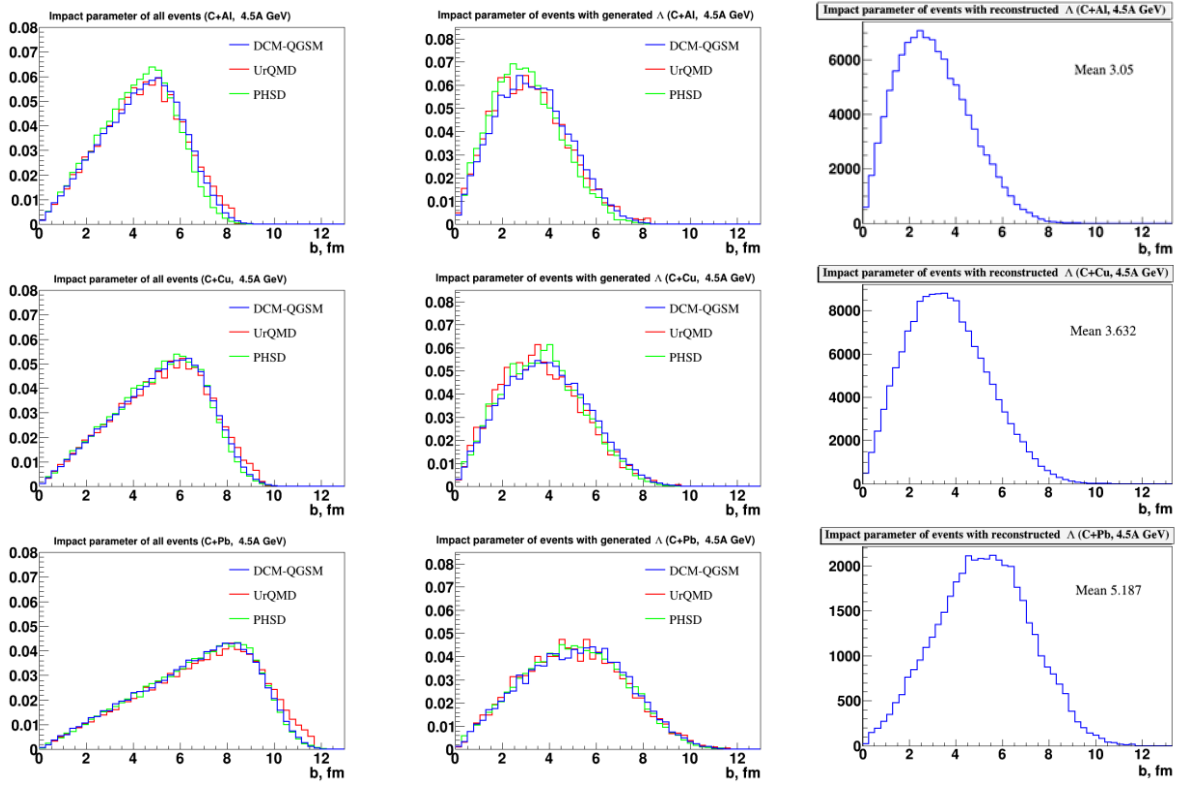


Fig. 12d. Impact parameter distributions of minimum bias interactions of 4.5 AGeV carbon beam with *C*, *Al*, *Cu*, *Pb* targets, generated with the DCM-QGSM, UrQMD and PHSD models (left). Impact parameter distribution of minimum bias events with generated  $\Lambda$  hyperons generated with DCM-QGSM, UrQMD and PHSD models (center). Impact parameter distribution of DCM-QGSM minimum bias events with reconstructed  $\Lambda$  hyperons (right).

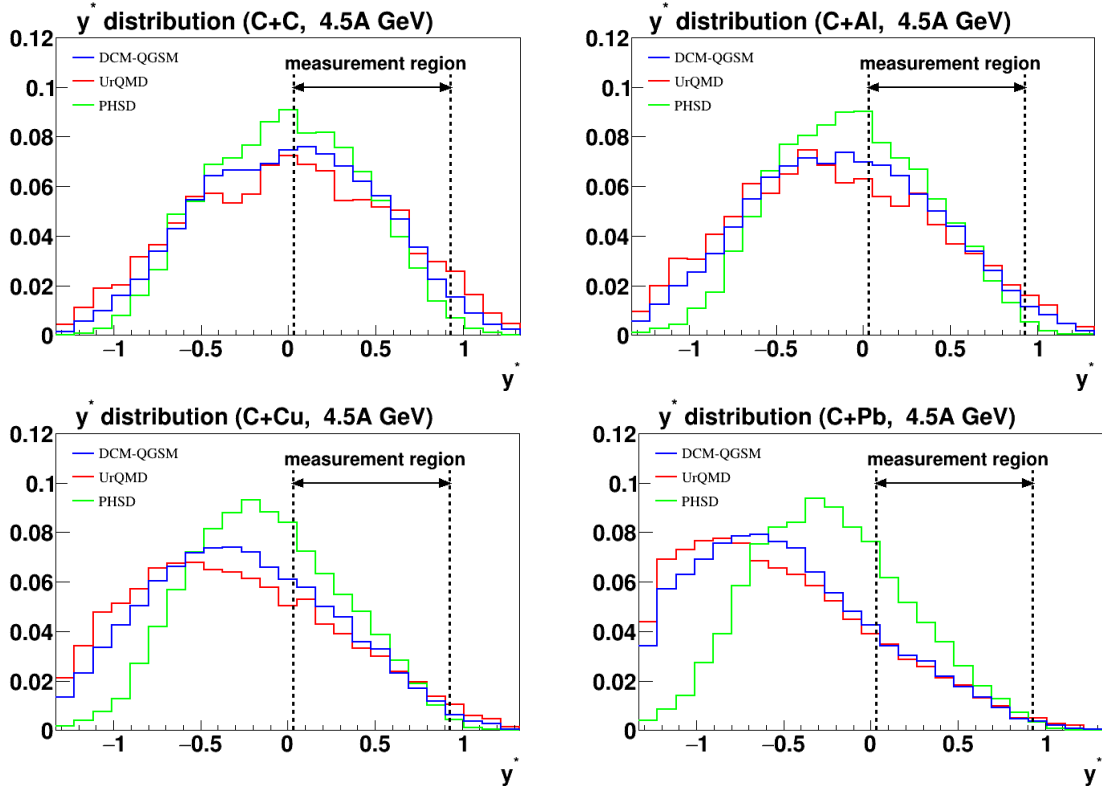


Fig.12e. Rapidity spectra of  $\Lambda$  hyperons in minimum bias interactions of 4.5 AGeV carbon beam with *C*, *Al*, *Cu*, *Pb* targets, generated with the DCM-QGSM, UrQMD and PHSD models. The BM@N measurement range in  $y^*$  is indicated.



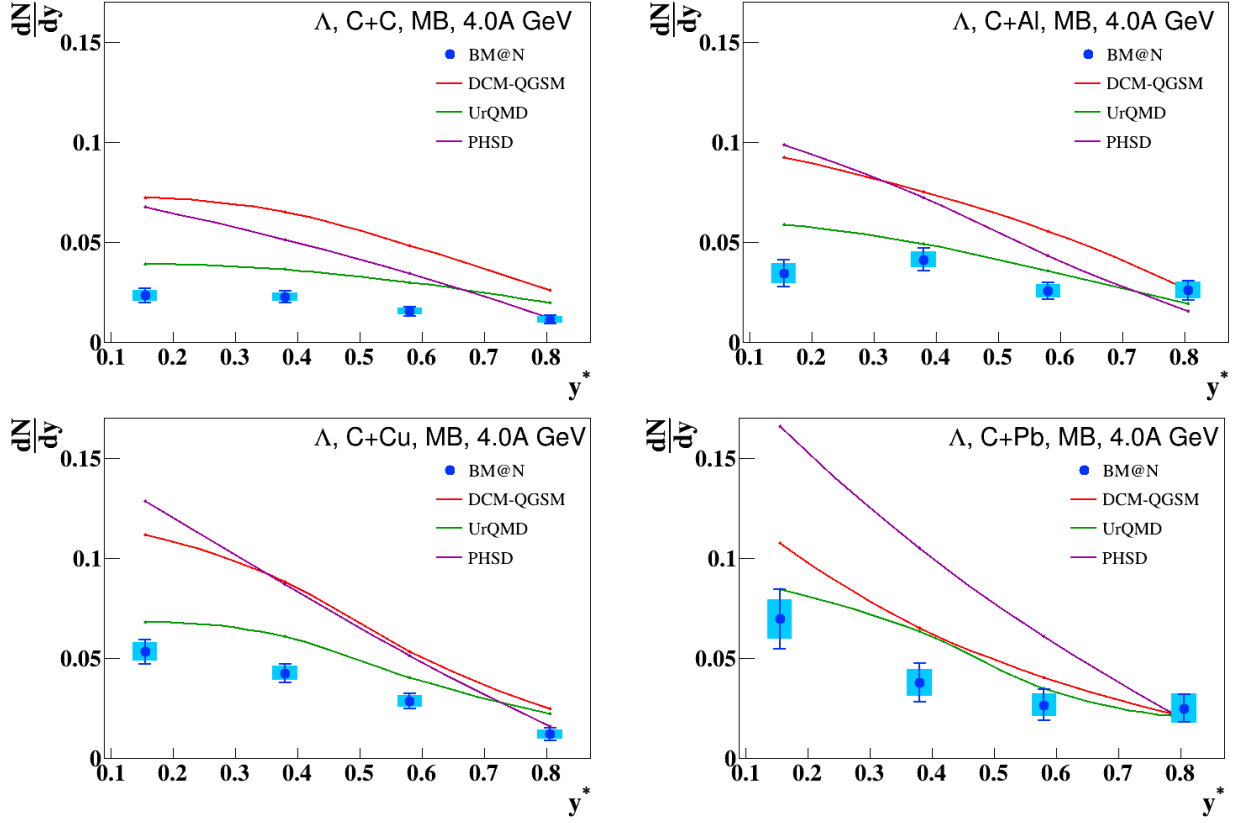


Fig. 13a. Reconstructed rapidity  $y^*$  spectra of  $\Lambda$  hyperons in minimum bias  $C+C$ ,  $C+Al$ ,  $C+Cu$ ,  $C+Pb$  interactions at 4.0 AGeV carbon beam energy (blue crosses). Predictions of the DCM-QGSM, UrQMD and PHSD models are shown as red, green and magenta lines.

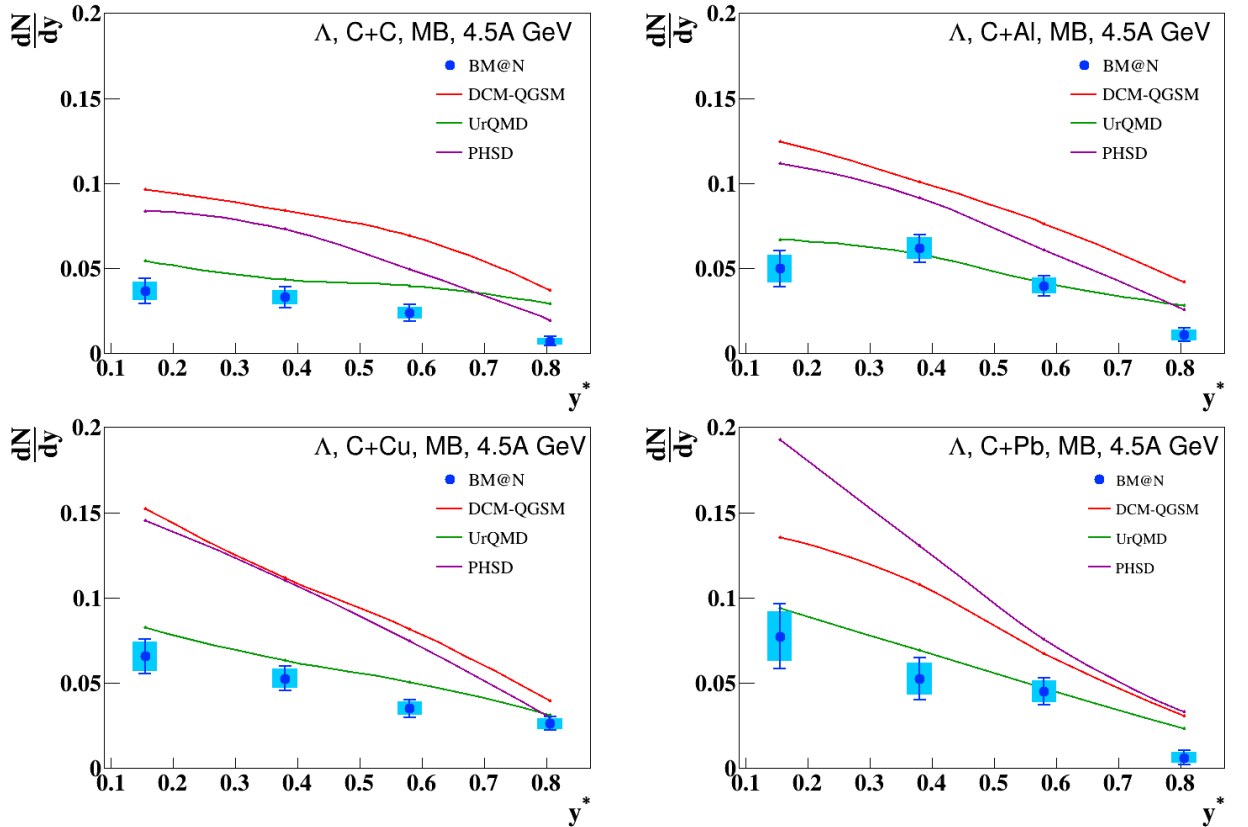
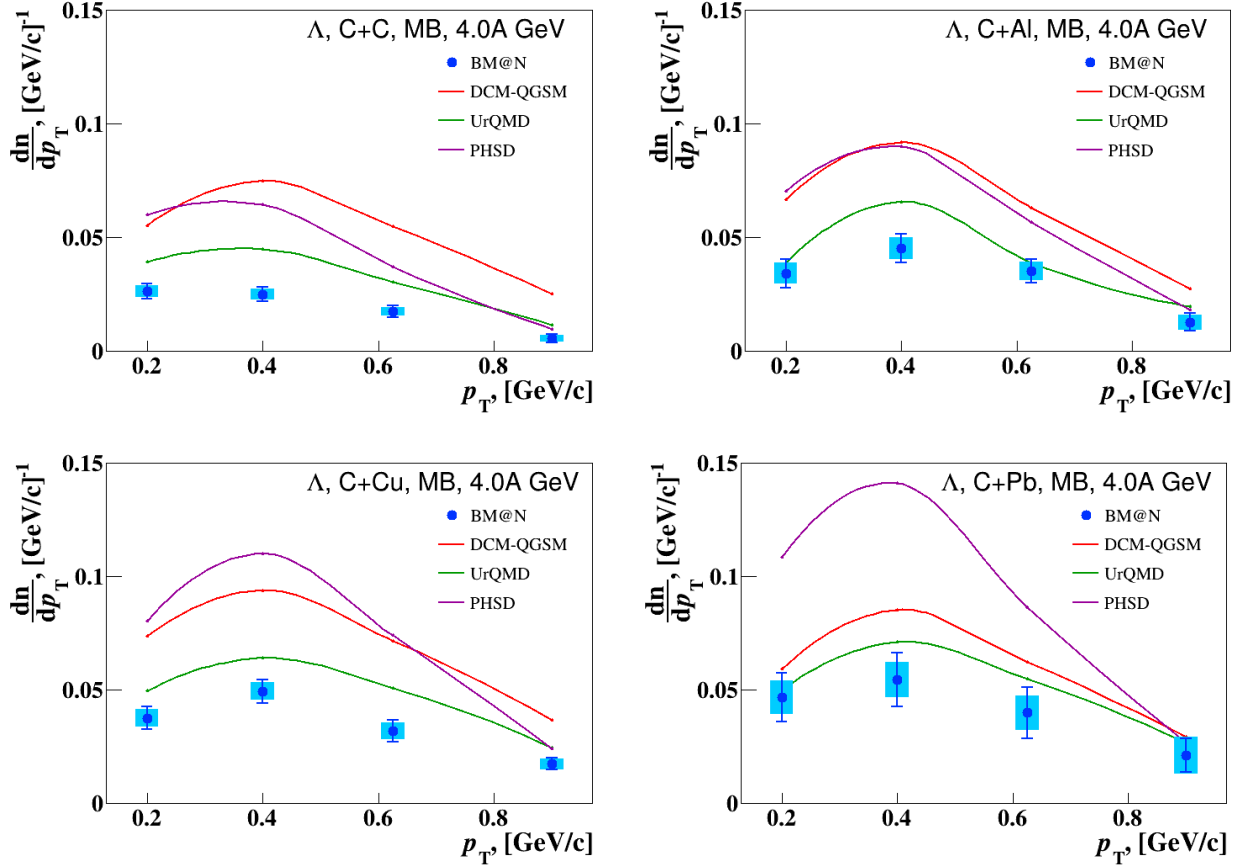


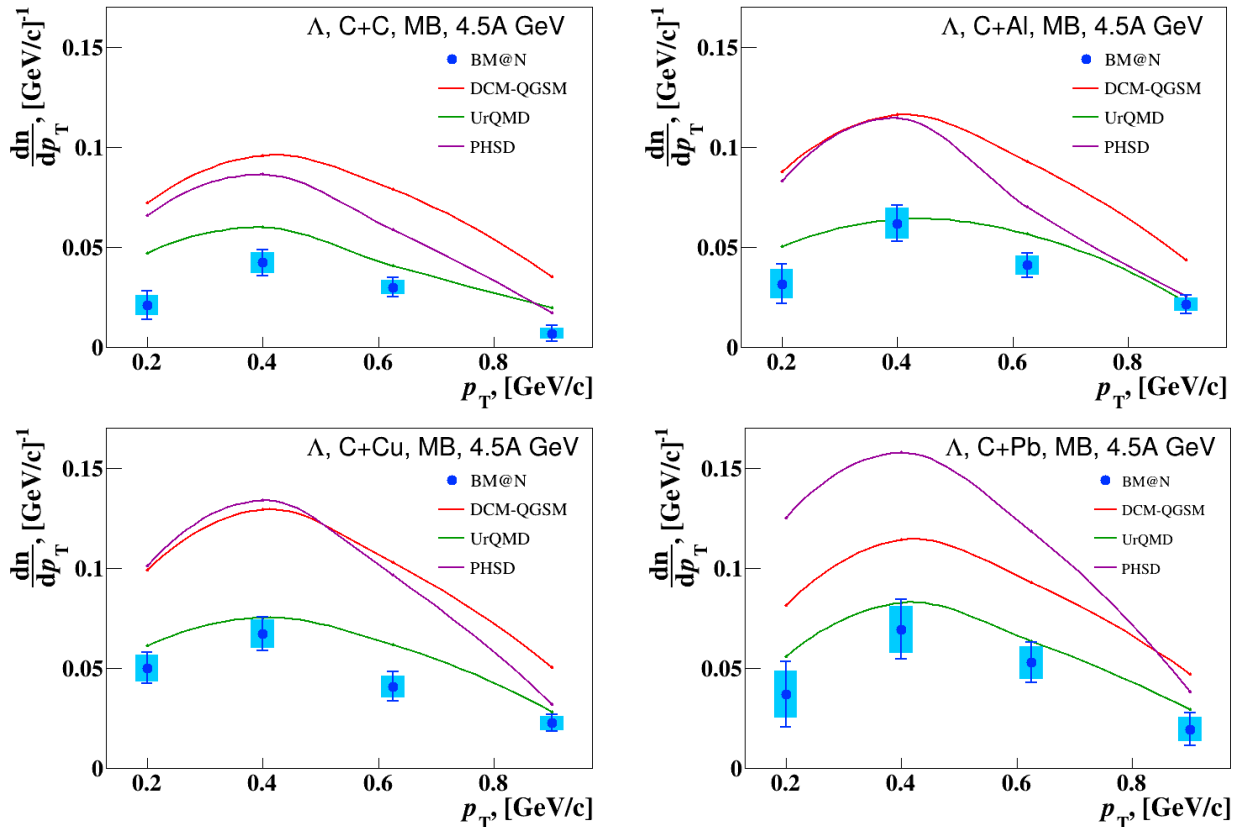
Fig. 13b. Reconstructed rapidity  $y^*$  spectra of  $\Lambda$  hyperons in minimum bias  $C+C$ ,  $C+Al$ ,  $C+Cu$ ,  $C+Pb$  interactions at 4.5 AGeV carbon beam energy (blue crosses). Predictions of the DCM-

QGSM, UrQMD and PHSD models are shown as red, green and magenta lines.



326

Fig.14a. Reconstructed transverse momentum  $p_T$  spectra of  $\Lambda$  hyperons in minimum bias  $C+C$ ,  $C+Al$ ,  $C+Cu$ ,  $C+Pb$  interactions at 4.0 AGeV carbon beam energy (blue crosses). Predictions of the DCM-QGSM, UrQMD and PHSD models are shown as red, green and magenta lines.



327

Fig. 14b. Reconstructed transverse momentum  $p_T$  spectra of  $\Lambda$  hyperons in minimum bias  $C+C$ ,

$C+Al$ ,  $C+Cu$ ,  $C+Pb$  interactions at 4.5 AGeV carbon beam energy (blue crosses). Predictions of the DCM-QGSM, UrQMD and PHSD models are shown as red, green and magenta lines.

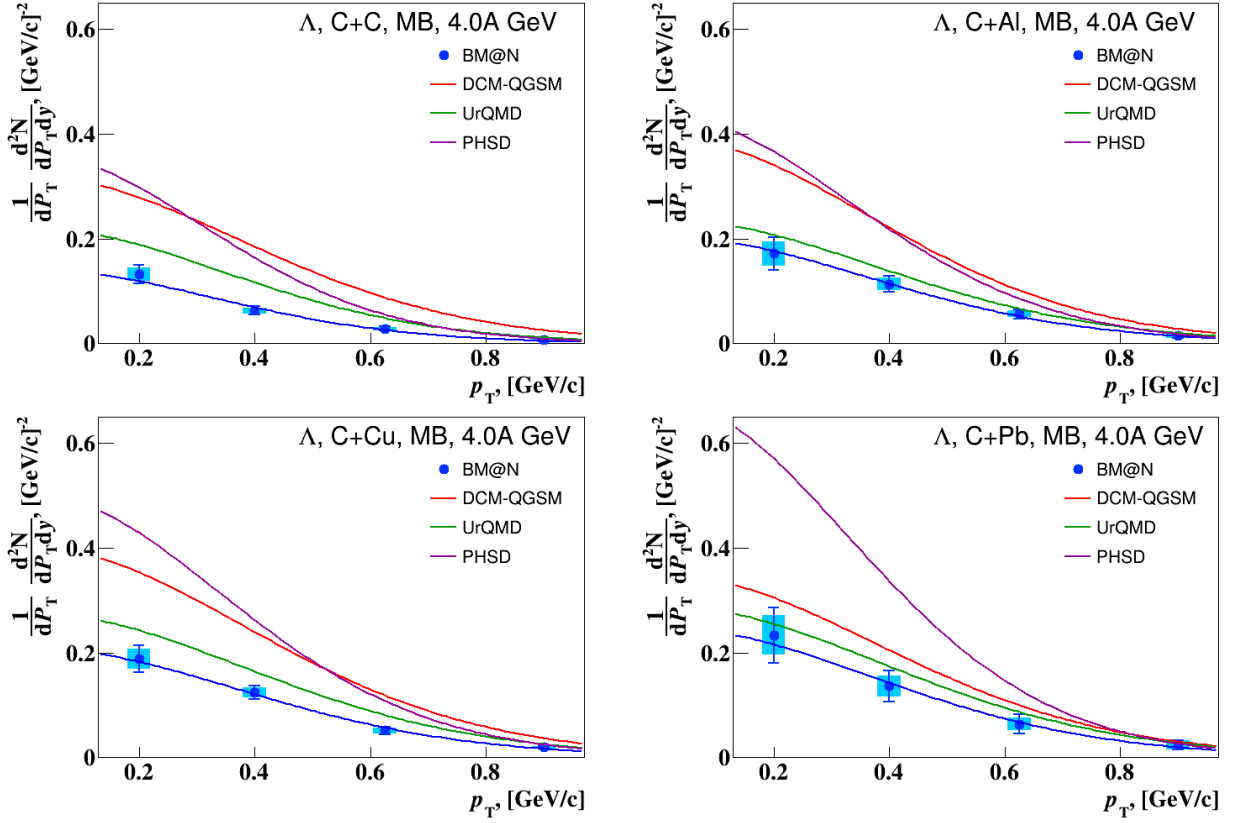


Fig. 15a. Invariant transverse momentum  $p_T$  spectra of  $\Lambda$  hyperons in minimum bias  $C+C$ ,  $C+Al$ ,  $C+Cu$ ,  $C+Pb$  interactions at 4.0 AGeV carbon beam energy (blue crosses). The error bars represent the statistical errors, the blue bands show the systematic errors. Predictions of the DCM-QGSM, UrQMD and PHSD models are shown as red, green and magenta lines.

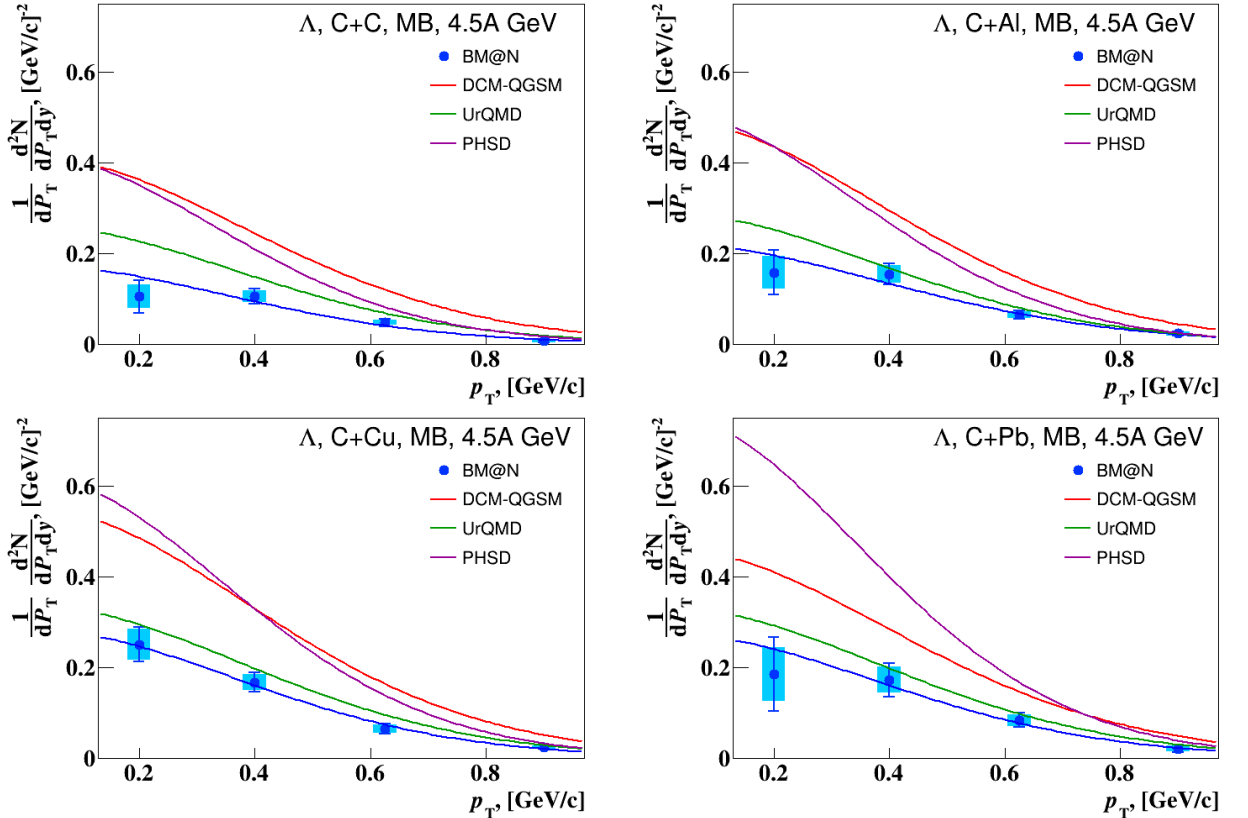


Fig. 15b. Invariant transverse momentum  $p_T$  spectra of  $\Lambda$  hyperons produced in minimum bias

$C+C$ ,  $C+Al$ ,  $C+Cu$ ,  $C+Pb$  interactions at 4.5 AGeV carbon beam energy (blue crosses). The error bars represent the statistical errors, the blue bands show the systematic errors. Predictions of the DCM-QGSM, UrQMD and PHSD models are shown as red, green and magenta lines.

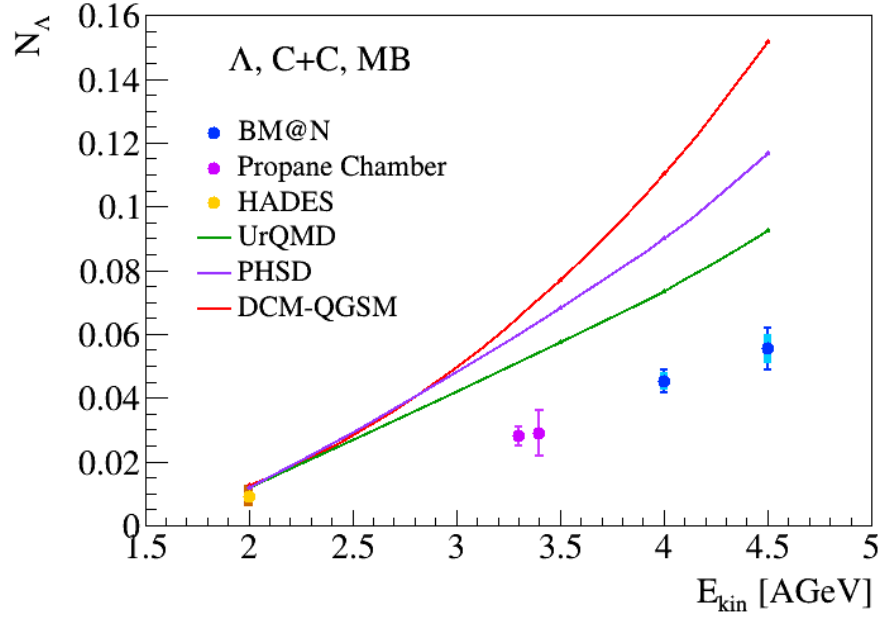


Fig.16a. Energy dependence of  $\Lambda$  yields measured in different experiments. The error bars represent the statistical errors, the blue bands show the systematic errors. BM@N result is compared with data taken from [ArakelianCC], [ArmutCC], [HadesL0]. The predictions of the DCM-QGSM, UrQMD and PHSD models are shown as colored lines.

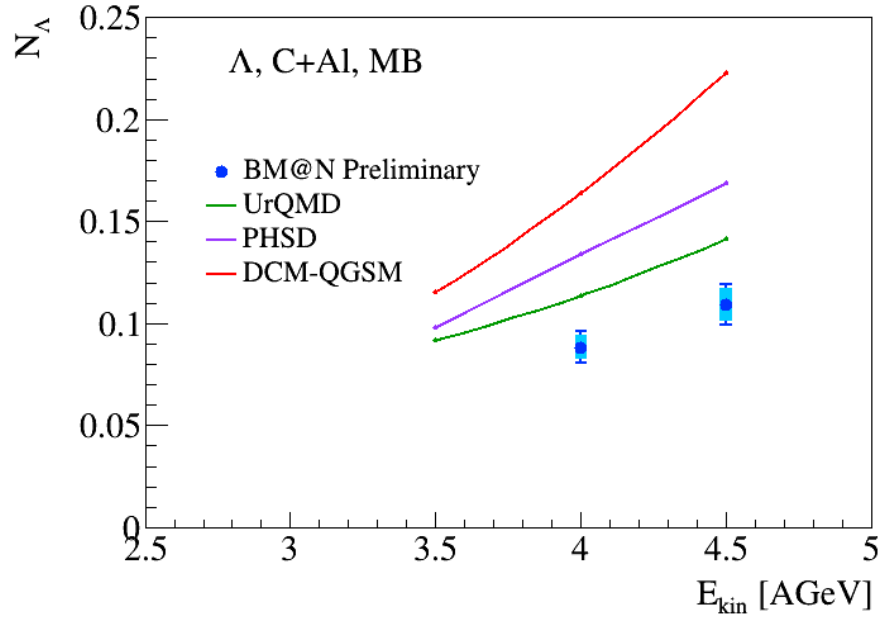


Fig.16b. Energy dependence of  $\Lambda$  yields measured in BM@N  $C+Al$  minimum bias interactions. The error bars represent the statistical errors, the blue bands show the systematic errors. The predictions of the DCM-QGSM, UrQMD and PHSD models are shown as colored lines.

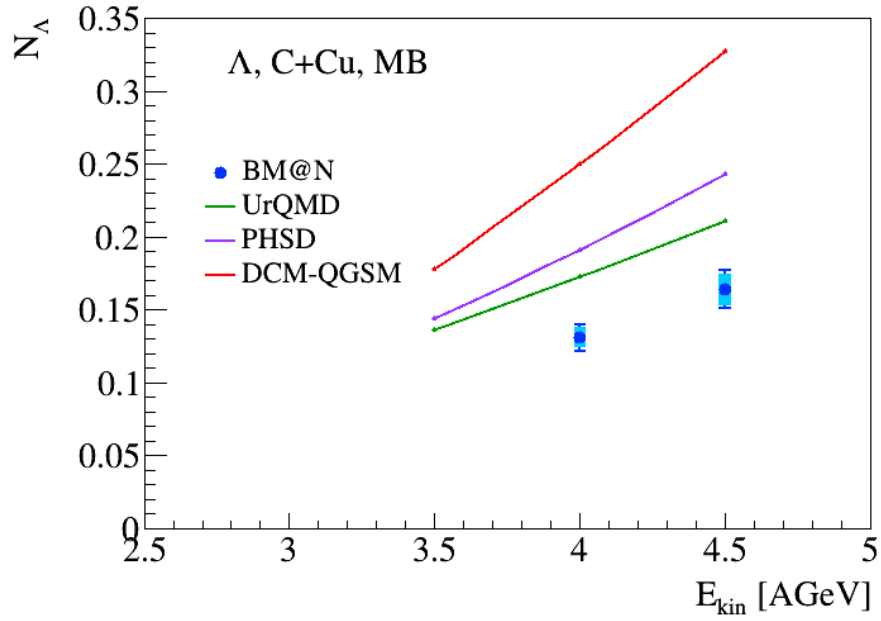


Fig.16c. Energy dependence of  $\Lambda$  yields measured in BM@N  $C+Cu$  minimum bias interactions. The error bars represent the statistical errors, the blue bands show the systematic errors. The predictions of the DCM-QGSM, UrQMD and PHSD models are shown as colored lines.

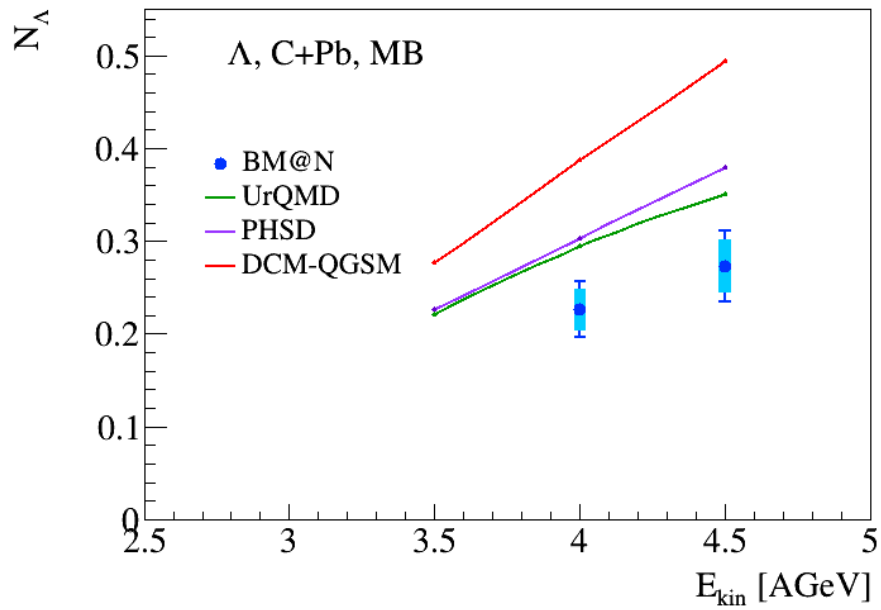


Fig.16d. Energy dependence of  $\Lambda$  yields measured in BM@N  $C+Pb$  minimum bias interactions. The error bars represent the statistical errors, the blue bands show the systematic errors. The predictions of the DCM-QGSM, UrQMD and PHSD models are shown as colored lines.

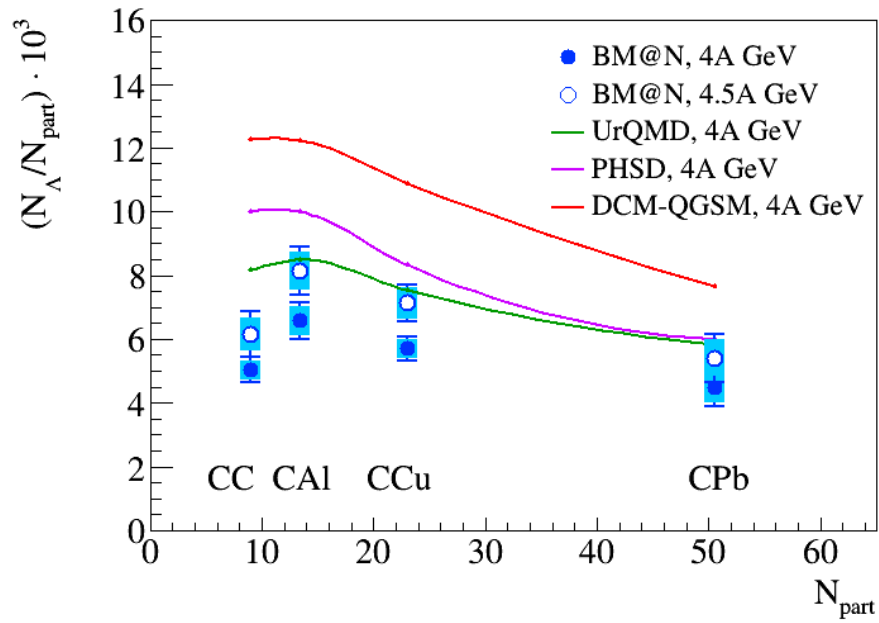


Fig.17. Ratios of the  $\Lambda$  hyperon yields to the number of nucleons-participants measured in BM@N carbon-nucleus interactions at 4.0 and 4.5 AGeV. The error bars represent the statistical errors, the blue bands show the systematic errors. The predictions of the DCM-QGSM, UrQMD and PHSD models are shown as colored lines.